Dynamics of core-mantle separation: Influence of viscosity contrast and metal/silicate partition coefficients on the chemical equilibrium

V. Clesi, J. Monteux, B. Qaddah, M. Le Bars, J.-B. Wacheul, Mohamed Ali M.A. Bouhifd

▶ **To cite this version:**

V. Clesi, J. Monteux, B. Qaddah, M. Le Bars, J.-B. Wacheul, et al.. Dynamics of core-mantle separation: Influence of viscosity contrast and metal/silicate partition coefficients on the chemical equilibrium. Physics of the Earth and Planetary Interiors, 2020, 306, pp.106547. 10.1016/j.pepi.2020.106547 . hal-02933230

HAL Id: hal-02933230
https://uca.hal.science/hal-02933230

Submitted on 5 Nov 2020

HAL is a multi-disciplinary open access archive for the deposit and dissemination of scientific research documents, whether they are published or not. The documents may come from teaching and research institutions in France or abroad, or from public or private research centers.

L'archive ouverte pluridisciplinaire **HAL**, est destinée au dépôt et à la diffusion de documents scientifiques de niveau recherche, publiés ou non, émanant des établissements d'enseignement et de recherche français ou étrangers, des laboratoires publics ou privés.

Dynamics of core-mantle separation:

Influence of viscosity contrast and metal/silicate partition coefficients on the chemical equilibrium

V. Clesi[a,*], J. Monteux[a], B. Qaddah[a,b], M. Le Bars[b], J.-B. Wacheul[b], M.A. Bouhifd[a]

[a]Université Clermont Auvergne, CNRS, IRD, OPGC, Laboratoire Magmas et Volcans, F-63000 Clermont-Ferrand, France

[b]CNRS, Aix Marseille Université, Centrale Marseille, Institut de Recherche sur les Phénomènes Hors Equilibre, UMR 7342, 49, Rue F. Joliot-Curie - B.P. 146, 13384 Marseille Cedex 13, France

*Corresponding author: vincent.clesi@univ-lyon1.fr

Present address: Laboratoire de Géologie de Lyon- Terre, Planètes, Environnement, CNRS UMR 5276, ENS de Lyon, Université Lyon 1. Campus de la Douà, Batiment Geode, 2 Rue Raphaël Dubois, 69622 Villeurbanne Cedex.

Abstract

The composition of the Earth's core and mantle is set by the chemical equilibrium between metals and silicates during core/mantle segregation. The metallic core separated from the mantle by gravitational descent in the form of diapirs in a magma ocean, and therefore the dynamics of the diapir's downward movement has an influence on the chemical equilibrium. In this study, we characterize the descent of metallic droplets into a molten silicate using numerical models. By varying the silicate and metal viscosities (between 0.1 and 1000 Pa.s for each phase) as well as the partition coefficient between metal and silicate ($D^{met/sil}$, varying between 1 and 1000), we obtained quantifying parametrizing equations for the degree of equilibrium between molten metal and molten silicate, in a regime characterized by low *We* (*We* < 10) and low *Re* (10^{-3}<*Re*<10^{2}). We showed that the main parameters controlling the equilibrium for a siderophile element are the viscosity of the silicate and the partition coefficient. We applied our parameterization for Ni and Co in the context of late accretion on Earth so as to quantify the variation of the Ni/Co ratio after a large impact as a function of the magma ocean viscosity, for an iron-rain scenario of metal/silicate segregation. Using previous models (Canup, 2004) of the Moon–forming impact, we showed that the Moon formation had an effect on the current Ni/Co ratio. Depending on the radius of Theia's core and the viscosity of the magma ocean produced after the impact between the proto-Earth and Theia, the Moon formation could account for 0.45 % to 3 % of the current Ni/Co ratio for magma ocean viscosities of 0.1 to 100 Pa.s, respectively.

1. Introduction

The main process occurring on Earth during the first 100-150 million years was the segregation of its metallic Fe-rich core (*e.g.* Bouhifd et al., 2017; Rubie et al., 2015; Wood et al., 2006; and references therein). One major consequence of this segregation is the depletion of the Earth's mantle in the siderophile elements relative to primitive solar system abundances (*e.g.* Jones and Drake, 1986).

The most recent Earth core formation models include a combination of multistage core-mantle differentiation with N-body accretion simulations, combined with continuous Earth core formation where pressure, temperature, oxygen fugacity and chemical composition of both the mantle and core vary during accretion of the Earth (*e.g.* Rubie et al., 2015, and references therein). These models consider that the accretion of the Earth occurred during a series of large impact events (*e.g.* Canup, 2008; Wetherill, 1985; O'Brien et al., 2006; Monteux et al., 2009; Nakajima and Stevenson, 2015). More importantly, these models provide results for the metal-silicate partitioning of a significant number of siderophile elements, which are consistent with observed mantle abundances given that the oxygen fugacity increases from about IW-5 to IW-2 (5 to 2 log units lower than the Iron-Wüstite buffer) during core segregation (*e.g.* Cartier et al., 2014; Rubie et al., 2015; Wade and Wood, 2005).

In this context, the behavior of Ni and Co (two refractory and moderately siderophile elements) has been considered to provide an important indication of the conditions of

Earth core formation. The consensus is now that metal-silicate equilibration at high pressure, in the range of 40 – 60 GPa (corresponding to depths of 1000 – 1500 km), was required to produce the observed Ni and Co depletions in the mantle (Bouhifd and Jephcoat, 2011; Siebert et al., 2012; Righter, 2011; Fischer et al., 2015; Clesi et al., 2016, for some of the most recent studies). Similar conclusions were reached based on the metal-silicate partitioning of lithophile and weakly-siderophile elements (*e.g.* Mann et al., 2009). One can note here that the conditions of Earth core formation as derived from metal-silicate partitioning of several elements cannot be used as an argument for single-stage core formation. This is highly unlikely given that Earth core formation occurred over a series of large impact events.

Most core formation models are based on metal-silicate partitioning experiments where both phases are fully molten and both thermodynamic and kinetic equilibrium are reached. This type of scenario favors rapid core - mantle segregation, which is confirmed by isotopic studies on Hf/W and short lived isotopes (Kleine et al., 2002; Jacobsen et al., 2008). If the kinetic equilibrium is well constrained, the extent to which the mantle and core equilibrate with each other is model dependent. So we know that if the metal were to segregate by forming large diapirs descending through the silicate magma ocean, the timescale for the equilibration would be too long to explain the isotopic ratios of Hf/W (Rubie et al., 2003). Therefore, the metal could have segregated by forming smaller diapirs, or droplets, whose radius varied between 0.1 to 10 cm, forming a cloud of iron in

80 the magma ocean (Deguen et al., 2014; Wacheul et al., 2014). An intermediate scenario
81 combining iron-rain mingling for the first part of segregation in the magma ocean,
82 followed by creation of large descending diapirs also exists, which can explain the
83 equilibrium in a deep magma ocean. In such a scenario, the metal falls through the molten
84 silicate in the form of droplets, and then forms a metallic pond at the base of the magma
85 ocean. Gravitational instability then allows metal to form large diapirs which descend
86 through the solid layer of the mantle into the proto-core (*e.g.* Stevenson, 1981, Monteux
87 et al., 2015, Fleck et al., 2018). This study focuses on the iron-rain phase of core-mantle
88 segregation, during which chemical equilibrium is reached (Rubie et al., 2003, 2011), as
89 large diapirs have less chemical interaction with the surrounding fluid (Ulvrova et al.,
90 2011; Wacheul et al., 2014). In the scenario of segregation by iron rain (Fig. 1), the extent
91 to which the magma ocean is in equilibrium with the core depends on the properties of the
92 metallic flow. The physics of the fluid flow is dependent on various parameters, one of the
93 most important being the viscosity of the surrounding fluid (Ke and Solomatov, 2009;
94 Monteux et al., 2009; Ricard et al., 2009). Numerical and analog simulations of a metallic
95 diapir descending through a surrounding fluid with different viscosities have shown that
96 the diapir is more stable when surrounding viscosity increases from low values ($\sim 10^{-1}$
97 Pa.s) to high values ($\sim$ 100 Pa.s), (Samuel, 2012; Wacheul et al., 2014). This has an impact
98 on chemical equilibrium, since break–up of the diapir increases the surface of exchange
99 between metal and silicate and small droplets sink more slowly than large diapirs (Ulvrova

et al., 2011; Wacheul et al., 2014). The efficiency of equilibrium is also increased when internal convection favors homogenization of concentrations in the metallic droplets (Ulvrova et al., 2011).

The goal of the present study is to characterize the influence of viscosity (metal and silicate phases) and chemical equilibrium on the global equilibrium rate in a magma ocean. To do that, the most relevant methods are analog and numerical modeling (e.g. Samuel and Tackley, 2008; Sramek et al., 2010; Deguen et al., 2011; Wacheul et al., 2014). Numerical simulations are more practical than analog ones for studying the effects of different phenomena happening simultaneously. In addition, it is difficult to find analogs for both metal and silicate which will react exactly like these two phases, and even more complicated to find analogs that behave chemically and physically in the same way as molten metal and molten silicate. Given the limitations of analog experiments for multiple physical modeling, we chose to perform numerical simulations of a falling metallic sphere into a molten silicate using COMSOL Multiphysics 5.0 modeling software. This approach allows the chemical equilibrium for different types of siderophile elements to be determined. In our simulations we combined chemical diffusion calculations with different types of flow. In particular, these simulations led us to explore the contamination of a silicate column by an excess of a siderophile element initially present in the diapir. Since viscosity influences the type of flow, which in turn is crucial in core-mantle equilibrium modeling (Rubie et al., 2003; 2011; Samuel, 2012), viscosity must have an influence on

120 the extent of core-mantle equilibrium. Furthermore, the equilibrium depends on the
121 partition coefficients of the elements between metal and silicate ($D^{met/sil}$), which depend
122 on pressure, temperature, oxygen fugacity and composition of metal and silicate.
123 Therefore, we tested the contamination of silicate by generic siderophile elements using
124 four different values of $D^{met/sil}$ (1, 10, 100, 1000).

125 Since major chemical transfers likely occurred during the iron rain process (Rubie et
126 al., 2003) our simulations looked at the equilibrium of droplets with the surrounding
127 silicate. In general, large diapirs in a turbulent environment tend to break into small
128 droplets, forming a cloud in which each droplet moves at the same speed (Wacheul and
129 Le Bars, 2017, 2018). In this study, we look at how one droplet of a given radius (R_{Fe} = 1
130 cm), which can be deformed but cannot break (see Wacheul et al., 2014), interacts with
131 the surrounding silicate. Then this behavior is extrapolated to the entire droplet cloud, and
132 we can estimate the extent to which equilibrium is reached between the magma ocean and
133 the falling metal during planetary accretion.

134 As a result of these simulations, we constrain the chemical exchanges between a small
135 metallic diapir and a silicate volume as a function of silicate viscosity (varying from 0.1
136 Pa.s to 1000 Pa.s), the viscosity ratio between metal and silicate, and time. We thus
137 parameterize the effect of varying viscosity on metal-silicate equilibration, and we use this
138 parameterization to re-evaluate models of core-mantle segregation. Moreover, we
139 characterize the effect of changing the magma ocean viscosity on the chemical

composition of the mantle. Finally, we discuss the potential consequences of giant impacts such as the Moon-forming impact on the chemical composition of the Earth's mantle.

2. Physical Model

To model the sinking of a metallic droplet into a silicate liquid, we used the software COMSOL Multiphysics, and in particular the modules "Computational Fluids Dynamics" and "Chemical Reaction Engineering". In each module, a set of equations is defined and solved at each time step. These equations are described in the following subsections. The parameters we used for these equations are listed in Table 1.

2.1. Two-phase flow model

In our study, the fluid dynamics are governed by the Navier-Stokes equations that characterize:

- Conservation of mass

$$\nabla \cdot \boldsymbol{u} = 0 \tag{1}$$

- Conservation of momentum

$$\rho \frac{\partial \boldsymbol{u}}{\partial t} + \rho(\boldsymbol{u} \cdot \nabla)\boldsymbol{u} = -\nabla P\boldsymbol{I} + \nabla \cdot [\mu(\nabla \boldsymbol{u} + (\nabla \boldsymbol{u})^T)] + \rho \boldsymbol{g} + \boldsymbol{F_{st}} \tag{2}$$

158 Equation 1 is the conservation of mass for an incompressible fluid with $\boldsymbol{u}$ the flow
159 velocity **vector**. Equation 2 describes the conservation of momentum, with acceleration of
160 the fluid $(\frac{\partial \boldsymbol{u}}{\partial t})$ and an inertia term $(\rho(\boldsymbol{u}\cdot\nabla)\boldsymbol{u})$ where ρ is fluid density. The first term on
161 the right-hand side of Eq. 2 $(-\nabla P)$ is the effect of the dynamic pressure P on the fluid.
162 The second term $(\nabla\cdot[\mu(\nabla\boldsymbol{u}+(\nabla\boldsymbol{u})^T)])$ is the component representing the effect of
163 viscous forces on the fluid with μ the fluid viscosity. The third term $(\rho\boldsymbol{g})$ is the
164 gravitational force that applies to the whole domain with $\boldsymbol{g}$ the gravitational acceleration
165 **vector**. The fourth term $\boldsymbol{F_{st}} = \nabla\cdot(\sigma(\boldsymbol{I}-\boldsymbol{n}\boldsymbol{n}^T)\delta)$ is the surface tension force with σ the
166 surface tension coefficient, **I** the identity matrix, $\boldsymbol{n}$ a unit vector normal to the surface of
167 interest and δ a smeared out Dirac function located at the interface. Since the volume of
168 metal is small, we ignored the Coriolis forces in Eq. 2.
169 We monitored the interface between the liquid iron droplet and the molten silicates using
170 the Level Set method, a Eulerian and implicit method used in multiphase flow problems
171 (e.g. Qaddah et al., 2019). For that, we defined a function Φ, characterizing the silicate
172 when Φ = 0 and the metal when Φ = 1. The boundary between the two phases was then
173 set at Φ = 0.5. These values were obtained by modifying the level set field using a smeared
174 out Heaviside function (Olsson & Kreiss, 2005), which allows direct calculation of the
175 volume fraction of a given phase by integration of the variable Φ on the volume
176 considered. The equation governing the transport of Φ is:
177

$$\frac{\partial \Phi}{\partial t} + \boldsymbol{u} \cdot \nabla \Phi = \gamma \nabla \left(\epsilon_{ls} \nabla \Phi - \Phi(1-\Phi) \frac{\nabla \Phi}{|\nabla \Phi|} \right) \quad (3)$$

with γ (m/s) and ϵ_{ls} (m) the reinitialization parameters. The γ parameter limits the numerical diffusion of the metallic phase during the simulation and needs to be adjusted empirically when the viscosity varies. Indeed, γ is a parameter that determines the amount of reinitialization or stabilization and must be carefully adjusted for each specific problem. If γ is too low, the thickness of the interface might not remain constant, and oscillations in Φ could appear because of numerical instabilities. On the other hand, if γ is too high, the interface moves incorrectly. The ideal value of γ was given by the maximum velocity reached by the diapir during its descent, as detailed in section 3. The range of values for γ is given in Table 1. ϵ_{ls} is the parameter controlling the width of the interface between fluids during reinitialization. This equation (Eq. 3) is a combination of the equations presented in Olsson & Kreiss (2005), modified for the COMSOL in-built solver. This solver allows the advection (on the left-hand side of the equation) and the reinitialization parameter (right-hand side of the equation) to be solved at the same time. The dynamic viscosity and the density are evaluated using the level set function and are defined by $\mu = \mu_{sil} + \Phi(\mu_{met} - \mu_{sil})$ and $\rho = \rho_{sil} + \Phi(\rho_{met} - \rho_{sil})$, respectively (subscript *met* refers to metal and *sil* to silicates). The resolution of the level set equation without using the COMSOL Multiphysics module is detailed in Olsson & Kreiss, 2005. Furthermore, this method has been already validated and applied to a similar problem in Qaddah et al., 2019.

198

199 The temperature of both the metallic droplets and the surrounding molten silicates is
200 difficult to constrain. It is related to the history of both phases before the merging and
201 involves radioactive heating, viscous dissipation and accretionary heating. In our study
202 we consider that the impact that precedes the iron droplet sinking homogenizes the
203 temperature of both phases. Hence, we do not consider heat conservation in the equations
204 solved in our models, and focus instead on the chemical equilibration processes alone.

205

206

207 **2.2.** *Chemical model*

208 The chemical diffusion and reactions of elements are described by transport equations
209 including an advective term to account for the movement of the phase and conservation of
210 mass, a diffusion term (Fick's law) to account for diffusive transfer, and a reaction term
211 to account for the chemical transfer based on the partition coefficient between metal and
212 silicate. In our models we solve the following equation:

213 $$\frac{\partial c_i}{dt} + \nabla \cdot (-k_c \nabla c_i) + \boldsymbol{u} \cdot \nabla c_i = R_i \quad (4)$$

214 Eq. 4 is the transport equation for diluted species including Fick's law for the diffusion of
215 an element $\left(\nabla \cdot (-k_c \nabla c_i)\right)$ with the addition of an advective term $(\boldsymbol{u} \cdot \nabla c_i)$ to account for

motions within the fluids. c_i is the concentration of element *i* in the phase of interest, k_c the diffusion coefficient and R_i the reaction rate for element i.

In our case, there are no external sources of elements (N_i=0, Fig. 2).

We assumed the diffusion coefficient (k_c) to be the same for both phases, and independent of the partition coefficient (D_i). Therefore we defined two functions to describe the behavior of element *i* in each phase. One function (X_i^{sil}) describes the behavior of element *i* in the silicate, and therefore tends toward 0 when $\Phi = 1$, the other (X_i^{met}) described the behavior of element *i* in the metal and tends toward 0 when $\Phi = 0$. The combination of the two functions give us the global concentration of element *i* in our computational domain. The link between the two functions, the partitioning coefficient and the phase field is made by defining a reaction at the interface between the metal and silicate (i.e. when $\Phi = 0.5$): R_i is the reaction rate necessary to reach the chemical equilibrium defined by the metal-silicate partition coefficient of element i (D_i). D_i is the Nernst partition coefficient given by $D_i = \frac{X_i^{met}}{X_i^{sil}}$, where X_i^{met} is the mass fraction of element i in the metallic phase, and X_i^{sil} the mass fraction of the same element in the silicate phase at equilibrium. R_i is given by Eq. 5:

$$\frac{dc_i}{dt} = R_i \qquad (5)$$

Where c_i is the concentration in either silicate or metal in mol.m^{-3}, obtained from the density of the phase where the element is ρ^{phase} (for either a metal or silicate phase), the

molar mass of the element (M_i) and the mass fraction of the element i in the phase considered is represented by $c_i = {X_i^{phase} \rho^{phase}}/{M_i}$. R_i is automatically calculated in a stationary state from the initial conditions and a given partition coefficient so as to reach equilibrium using COMSOL's in-built solver before the simulation. The reaction rate is high enough to maintain the equilibrium between two calculation steps: the typical time for equilibration is 10^{-5} s, which is less than the time step solved by solver. R_i is negative when removing siderophile elements from the metallic phase, and positive when creating the same element in the silicate phase. The reaction function is only defined for the metal/silicate boundary, given by the condition $\Phi = 0.5$. The higher the value of $D_i^{met/sil}$, the closer the conditions are to equilibrium, and the lower the reaction rate (R_i) will be. For the domain where $\Phi = 0$ or 1, the equilibrium is set to 0, and therefore the reaction rate is 0. For a given time step, the in-built COMSOL Multiphysics 5.0 solver calculate the Navier-Stokes equations (Eqs. 1 and 2) using finite element method, yielding the velocity field. Then the level-set equation is computed at the same time the advection-diffusion (Eq. 4) equation is solved by finite-element methods on the entire computational domain, with the reaction R_i only defined where $\Phi = 0.5$. The results of the calculation are then used as starting condition for the next time step.

2.3. *Geometry, mesh and initial conditions*

First, we defined a geometry for the simulation, using one of the defined boundaries for the eulerian solver available with COMSOL Multiphysics 5.0 software geometries. The best choice for our type of simulation would have been be a 3-D model with a falling sphere inside it, so as to compare our simulation to analog simulations (Deguen et al., 2011, 2014; Wacheul et al., 2014). Since this type of simulation is very costly in terms of computational time, especially for fluid flow simulations, we used a 2D-axisymetric geometry, which solves the equation on a 2D surface, and uses the symmetry conditions to give a 3D output. This is a good compromise between a 2D and 3D simulation when the diapir is not fragmented. Our simulations focused on a weakly deformable falling sphere (i.e. no break up) with a radius of 1 cm in a cylinder whose diameter was set during the calibration of the simulation.

The geometry and boundary conditions used in this study are presented in Fig. 2. In this geometry, a rotational symmetry axis is defined. For the fluid flow, the boundaries of our calculation domain are characterized as follows:

- on the top boundary, the condition is given by P= 1 atm,
- on the bottom boundary, the condition is set to be a null velocity field
- on the side boundary, the condition is a no slip condition
- on all the boundary there is a no flow condition for the level set equation.

The conditions for chemical diffusion is a constant budget in chemical elements throughout the numerical simulation, i.e. no elemental flux (N_i = 0), inward or outward, is allowed on all the external boundaries.

For our calculation domain we used a fixed mesh of triangles, with three main parameters: h_{max}, h_{min} and a curving parameter. The h_{max} parameter gives the maximum size of the triangle side, h_{min} gives the minimum size and the curving parameter gives the arc interception for curving triangles at spherical boundaries. The parameter controlling the accuracy and the computation time for the calculation is h_{max}. The best value for this parameter was determined in the resolution study, see Section 2.4.

The initial conditions are described in Fig. 2. The viscosities were varied for each simulation, but the geometry of the set-up, the initial concentrations, the densities and the droplet radius were kept constant. To avoid numerical instabilities inherent in X_{sil}^0 = 0 %wt , the initial concentration was set to $X_{sil}^0 = 10^{-4}$ %wt for the silicate with a density ρ_{sil} = 3300 kg.m^{-3}; and X_{met}^0 = 20 % wt for the metal with a density ρ_{met} = 8000 kg.m^{-3}. The radius of the droplet was R_{Fe} = 1cm, falling in a cylinder with a 5 cm radius and a 28 cm height, with the center of the droplet placed initially at 26 cm height.

2.4. Tests of the COMSOL simulation

To correctly set up the computational domain in terms of size and mesh, two effects need to be accounted for:

(1) Grid resolution, which has to be sufficient to capture the physics of small droplet deformation.

(2) Boundary effects, to avoid a major influence of the outer border of the domain on the flow and the generation of artifacts in the velocity field.

To minimize the numerical diffusion of iron during the diapir's descent, we tested several maximum sizes for the mesh grid component $h_{max.}$ Fig. 3 illustrates the time evolution of the ratio between the calculated volume over the theoretical volume of one droplet (given by $V_{theoretical} = \frac{4}{3}\pi R_{Fe}^3$ with R_{Fe}=1cm) for h_{max} values ranging between 0.06 and 0.2 cm. The simulations were performed using the same initial geometry as in Fig. 2, with a silicate and a metal viscosity of 100 Pa.s (corresponding to a Reynolds number of ~2. 10^{-3}, see Eq. 6) and no chemical component to solve. The precision of the calculation increased as the mesh size decreased, especially when there was deformation. On the other hand, the smaller the mesh grid components were, the longer it took to complete the calculation. As can be seen in Fig. 3, the precision is better for a mesh component size of 0.1 cm than for smaller (0.06 and 0.08 cm) or larger (0.2 cm) mesh component sizes. In addition, a maximum component size allowed a calculation time of a few hours (~ 6 hours), whereas

a mesh grid size of 0.06 cm yielded calculation times from a dozen hours to 2 days for the less viscous flows. Therefore, for the rest of the study, we used a maximum size of 0.1 cm for the mesh grid (i.e. $R_{Fe}/10$). The mesh size could be adapted to the type of flow for each simulation: for example, for a higher degree of diapir deformation during the simulation (typically for less viscous flows), the mesh size had to be decreased to avoid numerical artifacts. To increase the precision, COMSOL also made it possible to set a minimum size for the mesh grid component so as to get an adapted mesh, with smaller elements at the interfaces between the two phases, and larger elements as the distance from the interface increases. Varying the parameter h_{min} did not affect the simulation for a given value of h_{max}, so it was kept at a constant value of $h_{min} = h_{max}/40$.

The second point was to avoid boundary effects on the fluid flow during the simulation. We tested several domain sizes and checked the different velocity field components (r- and z- components). We chose a height equal to $28xR_{Fe}$ and a width equal to $5xR_{Fe}$ which was sufficient to avoid the recirculating flow associated to the descending diapir having a large effect on the velocity field (Fig. 4), while keeping computational time within reasonable bounds. This size of domain still affected the velocity of the diapir (Chang, 1961 and Fig. 4). Fig. 4 shows that increasing the width to $6x\ R_{Fe}$ changed the velocity field, albeit very slightly, which indicates a diminution of the wall effect: the mean velocity of the diapir increased by 8 % compared to the mean velocity for a width of $5xR_{Fe}$.

However, increasing the width of the domain from $5xR_{Fe}$ to $6xR_{Fe}$ led to a significant increase in computational time (by at least 46 %). Given the limited effect of increasing the domain width and the significant effects on the computational time, we considered this smaller width to be suitable for the study. We applied the same reasoning to choose the height of our domain. To test the resolution of the diffusion in Eq. 4, we benchmarked the validity of the COMSOL solver against steady and unsteady analytical solutions for diffusion problems (Crank, 1975). To test the advective part, we compared the flow velocities from our models with those velocities obtained by Samuel (2012) (see section 3.2). Our results showed an acceptable agreement, despite a large discrepancy between theoretical results and observed velocities (45% for the largest one) for flows with the largest velocities, i.e. in the intermediate regime. To explain the observed differences, we calculated the mesh Peclet number Pe_{mesh} after each simulation with $Pe_{mesh} = \frac{vh_{max}}{k_c}$, where v is the velocity of the diapir, h_{max} is the mesh size and k_c is the diffusion coefficient (10^{-6} $m^2.s^{-1}$, which is higher than a typical chemical diffusion, but high enough to limit numerical diffusion (see Qaddah et al., 2020). In the reference case and for the other cases within the Stokes regime, the value of Pe_{mesh} was sufficiently low ($Pe_{mesh} < 10$) meaning that numerical diffusion was negligible (see Mittal & Jain, 2012). For the cases within the intermediate regime, Pe_{mesh} was higher ($Pe_{mesh} > 50$), which indicates possible numerical diffusion that likely affected our results. To correct this effect a much smaller mesh size would have been necessary. However, the mesh size necessary to prevent numerical

diffusion in our models would have led to unreasonable computational times. Therefore, for the lowest viscosity used in our models some error calculations might have occurred in our results, but are negligible in the final model (see Section 5 and 6).

3. Results

In this section we present the results of our simulations as well as a definition of the non-dimensional numbers and parameters used to interpret the results of the simulation in terms of degree of equilibrium. A reference run was arbitrarily defined to set a reference time evolution for the non-dimensional parameters. Then we varied the viscosity of the silicate and metallic phase for a given partition coefficient value, and finally we varied the value of the partition coefficient for a given viscosity.

3.1. Reference case and characteristic non-dimensional numbers

In this section we present the results for a reference case, where $\mu_{sil} = \mu_{met} = 100$ Pa.s. The temporal evolution of the reference case flow is presented in Fig. 5. This figure shows that for this case both the diapir deformation and the numerical diffusion are weak. The metallic droplet moves a distance of $10 \times R_{Fe}$ (10 cm) in 12.1 seconds.

To compare this flow to other flows with different viscosities, we need to use non-dimensional numbers. Since this study focuses on the viscosity variations and the characteristics of the flow, the Reynolds number (*Re*) is the more adequate non-dimensional number, which is given by Eq. 6:

$$Re = \frac{\rho_{sil} R_{Fe} v_{diapir}}{\mu_{sil}} \quad (6)$$

where ρ_{sil} is the density of the surrounding silicate, R_{Fe} is the initial radius of the diapir, v_{diapir} is the velocity of the diapir and μ_{sil} is the silicate viscosity (see Table 1). This number expresses the ratio of inertial forces to viscous forces. When $Re < 1$, the flow is considered to be a Stokes flow, which means that diapir deformation is limited during the descent. When $1<Re<500$, the flow is an intermediate flow between Newtonian and Stokes flow (Samuel, 2012). In our study, we did not investigate the case of $Re > 500$, which is a highly turbulent Newtonian flow.

The velocity of the diapir is strongly governed by the viscosity of the surrounding silicate, which affects the value of *Re* (*e.g.* Samuel, 2012, and references therein). In order to compare different values of the viscosity ratio $R_\mu = \mu_{met} / \mu_{sil}$, we defined the reference time for each calculation as the time necessary for a metallic droplet with radius R_{Fe} to move through a distance $d=10\times R_{Fe}$.

388 The other non-dimensional number which controls the flow is the Weber number
389 (*We*), which is the ratio of the inertial forces on the surface tension:

390 $$We = \frac{\rho_{sil} v_{diapir}^2 R_{Fe}}{\sigma} \quad (7)$$

391 with σ the surface tension (see Tab. 1 for value). The break-up of the diapir is controlled
392 by the Weber number (Wacheul et al., 2014). When $We < 6$ the diapir is stable in Stokes
393 and intermediate flows, and when $We > 6$ the surface tension is no longer high enough to
394 prevent the diapir breaking up (Wacheul and Le Bars, 2017). In this case and in the rest of
395 the present study, the diapirs are always stable with $We < 6$. For the reference case, the
396 diapir velocity is about $v_{diapir} \approx 8\times10^{-3}$ m.s^{-1}. This velocity yields low values of *Re* and *We*
397 (2.2×10^{-3} and 1.2×10^{-3}, respectively), which explains the diapir's stability during its
398 descent (see Fig. 5).
399
400 To study the chemical equilibrium between metal and silicate, we calculated a non-
401 dimensional concentration, or more precisely a non-dimensional mass fraction termed *X'*.
402 This non dimensional mass fraction was calculated so as to satisfy three conditions:
403 (i) If there is no change in the initial concentration in the silicate, *X*' is equal to 0
404 (no equilibrium at all)
405 (ii) If equilibrium is reached, *X*' is equal to 1.
406 (iii) *X'* is proportional to the concentration in the silicate ($X' \propto X$)

The first condition is reached if $X = X^0_{sil}$. Therefore *X*' = 0 implies a null numerator for *X'*, i.e. $X' \propto X - X^0_{sil}$. For the second condition, it is reached if $X = {X^{eq}_{met}}/{D^{met/sil}}$, by definition of the partition coefficient, where X^{eq}_{met} is the concentration of the element in the metallic phase at equilibrium. In our case, the element is a siderophile ($D^{met/sil} \geq 1$) and the initial concentration is high ($X^0_{met} = 0.2$). Therefore, at the end of the simulation we could approximate the equilibrium concentration by $X^{eq}_{met} \sim X^0_{met}$. Satisfying the condition *X*' = 1, with $X' \propto X - X^0_{sil}$ and the non-dimensionality of *X*' yield to the following formula given in Eq. 8:

$$X' = \frac{X - X^0_{sil}}{X^0_{met}/D^{met/sil} - X^0_{sil}} \quad (8)$$

X' is a useful parameter for tracking the evolution of concentration in a particular case, but it is not enough to quantify how much of the silicate is affected by a change in concentration. Moreover, this parameter is not suitable for comparing different studies, because it is strongly affected by the duration of the sinking. The evolution of the non-dimensional concentration, *X'*, in the reference case is shown in Fig. 6. Equilibrium in the silicate is reached when *X'* = 1 (area in red). This area forms a very narrow zone around the diapir, and most of the silicate is not chemically equilibrated with the metal, because the simulation run time is not long enough.

The parameter R_C is the ratio of the silicate volume that has reacted with the metal to the total volume of silicate. The definition is $R_c = V^{sil}_{reacted}/V^{sil}_{total}$, where $V^{sil}_{reacted}$ is the

426 volume of silicate where $X > \boldsymbol{X_{sil}^{0}}$; meaning R_C is the volume fraction of silicate that has
427 reacted with the metal. To visualize how the ratio is calculated, a representation of the
428 integrated volume is shown in Fig. 7. In this figure, the areas colored in red represent the
429 volume of silicate that has evolved in terms of chemical composition, while the areas in
430 blue represent that which has not been contaminated by the diapir's descent.

431 For each simulation, the volume chemically affected by the diapir's descent increases with
432 time. The time evolution of the R_C value for the reference case is shown in Fig. 8. R_C is
433 increasing with time following the same trend in each case. The difference is in the
434 absolute values of $D^{met/sil}$: the more elevated the value is, the closer the initial conditions
435 are to equilibrium conditions, which leads to a lower reaction rate.

436

437

438 **3.2. Range of *Re* and *We* values**

439 The aim of our models was to constrain the influence of the viscosity contrast between
440 the silicate and metallic phases. This led to a wide range of *Re* and *We* values in our
441 numerical simulations. The viscosity of the silicates surrounding the metal droplet controls
442 the flow regime and the sinking velocity. The evolution of the time necessary to reach the

distance of $10\times R_{Fe}$, which depends mostly on the silicate viscosity (Samuel, 2012 and references therein), is presented in Fig. 9. The higher the viscosity of the silicate, the longer it takes for the diapir to reach a set distance. The changes in flow regime result in different expressions for the diapir velocity. In our study, the range of *Re* values only allows Stokes regime flows (*Re* < 1) or intermediate regime flows (1<*Re*<500), with two different expressions for the diapir's velocity. In a Stokes flow the velocity is given by:

$$v_{Stokes} = \frac{2}{9}\frac{(\rho_{met}-\rho_{sil})gR_{Fe}^2}{\mu_{sil}} \quad (9)$$

For intermediate flows, the sinking velocity is given by:

$$v_{intermediate} = \sqrt[2]{\frac{(\rho_{met}-\rho_{sil})gR_{Fe}}{\rho_{sil}C_D}} \quad (10)$$

with C_D the drag coefficient. In our case, the drag coefficient is approximated by $C_D = \frac{12}{Re} + 0.3$, following Samuel (2012). From Eq. 10, we can also calculate the velocity in each drop flow regime: Stokes, intermediate, and Newton (e.g. Qaddah et al., 2019). The theoretical times associated with the velocity are compared to the actual times observed in simulations in Fig. 9. It shows a good agreement between theoretical and observed diapir velocity, despite some scatter. This scatter is consistent with the wall effect of our simulations: the variation in velocity observed in the Stokes flow is of the order of 10 %, which is consistent with the variation expected if the wall effect is negligible (see Section 2.4). Comparison with the typical equilibrium time from Wacheul et al. (2014) in Fig. 9 shows that, except for the intermediate flows, the fall time chosen in our study is long

462 enough to reach full equilibrium (or more than 90 % of equilibrium in some cases) inside
463 the metal, leaving the silicate as the limiting phase for equilibrium. The dispersion of the
464 obtained reference time (Eqs. 8 and 9) in Fig. 9 for a chosen value of μ_{sil} is considered
465 therefore as a negligible discrepancy in the rest of the study.

466 In Fig. 10 we plot the *Re* values as a function of the *We* values for each simulation (i.e.
467 for each viscosity contrast used in our calculations). The velocity of the diapir (v_{diapir}) used
468 to calculate *Re* and *We* is determined from our numerical models by the time necessary for
469 the diapir to move through a distance of $10\times R_{Fe}$. This time is dependent on the viscosity
470 and illustrated in Fig. 9. Fig. 10 (left) shows that in all our numerical simulations, the
471 metallic droplet is stable (i.e. no break up occurs) even though some models are in the
472 Stokes regime and others are in the Intermediate flow regime. In Fig. 10 (right) we
473 compare the range of values with the range of *We* and *Re* values relevant to the geological
474 context of a liquid metallic droplet sinking through a terrestrial magma ocean (Wacheul et
475 al., 2014). As shown in Fig. 10 (right), our range of values is limited compared to possible
476 geophysical values. Larger diapirs leading to high *Re* and *We* values are not considered in
477 our study, which focuses on small droplets in the iron rain scenario.
478

479 **3.3. Influence of the viscosity ratio**

480 The viscosity ratio is an important parameter controlling the dynamics of diapir
481 descent, both its shape (Qaddah et al., 2019) and stability (Wacheul et al., 2014). In this

482 section, we focus on the influence of the viscosity ratio R_μ $(=\mu_{met}/\mu_{sil})$ by varying the value
483 of the silicate viscosity for a given metal viscosity. Changing the viscosity of metal affects
484 its ability to deform and, hence, its terminal velocity, but this effect is not as strong as the
485 change in velocity implied by a change in ambient viscosity. This behavior is consistent
486 with the equation of diapir velocity in Stokes and intermediate flows (Eqs. (9) and (10)),
487 and is strongly dependent on the silicate viscosity. It is visible in Fig. 9, where a decrease
488 in silicate viscosity from 1000 Pa.s to 10 Pa.s (Stokes flows) leads to an increase in sinking
489 velocity from 10^{-3} m.s^{-1} to 0.1 m.s^{-1} for a metal viscosity of 1 Pa.s. For a constant silicate
490 viscosity of 10 Pa.s, a decrease of the metallic viscosity from 1000 Pa.s to 0.1 Pa.s only
491 increases the velocity from 0.05 to 0.1 m.s^{-1}. The viscosity ratio influences the sinking
492 velocity and, hence, affects the *Re* number and the flow regime, but not as strongly as the
493 silicate viscosity.

494 Fig. 11 illustrates the influence of the *Re* number on the silicate volume chemically
495 contaminated during the sinking of a metallic droplet with R_{Fe}=1cm. For each case, the
496 evolution of R_C is shown as a function of *Re*, and for a distance of 10 cm ($10\times R_{Fe}$). The
497 time corresponding to this distance is shown in Fig. 5 as a function of viscosity. Except
498 for the case with $D^{met/sil} = 10^3$, there is no linear correlation between $\log(R_C)$ and $\log(Re)$.
499 However, we clearly show a transition between the Stokes regime and the Intermediate
500 regime. In the Stokes regime flow, an increasing *Re* (i.e. a decreasing value of μ_{sil}) leads
501 to a significant decrease of R_C, while R_C values seem to reach a plateau when the flow

reaches the intermediate flow regime. Fig. 11 also shows that the approximation made by Rubie et al. (2003) to achieve an analytical solution for equilibrium is only valid for low *Re* flows (high silicate viscosity). As the density of the silicate is not significantly altered by the reaction, the parameter R_c (volume ratio of silicate equilibrated) can be compared to their parameter F_s (mass ratio of silicate equilibrated). For the lowest *Re* value, there is good agreement between our numerical data and the analytical calculation. However, extrapolating the analytical solution to higher *Re* flows leads to an overestimation of the equilibrated volume.

The R_C ratio is presented in Fig. 12 as a function of R_μ. A decrease in R_C is observed with an increase in R_μ (i.e. a decrease of μ_{sil}) for a given viscosity of the metallic phase. For the five parts of Fig. 12, which correspond to the five values of μ_{met}, the trend and the magnitude of the values of R_c are quite similar, meaning that the effect of the viscosity ratio is less important than the ambient viscosity, which governs the flow regime. For high values of R_μ, the same plateau phenomenon as seen in Fig. 11 is observed, which corresponds to lower silicate viscosity values (intermediate flow). In the Stokes regime, the sinking velocity scales with μ_{sil}^{-1} (Eq. (9)) while in the intermediate regime, the sinking velocity scales with C_D^{-1}. Given the expression of the drag coefficient (derived from Samuel, 2012; see Section 3.2), and the expression of *Re* (Eq. (6)), the sinking velocity in the intermediate regime scales with $(\rho_{sil}\mu_{sil})^{-0.5}$, as given by Eq. (10). Hence, R_μ has a

greater effect on Stokes flows than intermediate flows, because the changes in diapir velocity are more pronounced for Stokes flows, as shown in Fig. 5.

Although the evolutions of R_C as a function of R_μ are quite similar in the five panels of Fig. 12, some differences are noticeable. For the lowest values of $\mu_{met,}$ the R_C ratio increases at high R_μ values while for high values of $\mu_{met,}$ the R_C ratio is nearly constant or decreases with high R_μ (except for $D^{met/sil}$ =1000). This could be explained by the fact that a higher viscosity ratio tends to stabilize the diapir and slow down its descent (Wacheul et al., 2014). In a Stokes regime, it leads to an increase in the time necessary to reach the same distance, in other words a longer reaction time; but in intermediate regimes this time does not change significantly, while the diapir is less deformed, leading to a smaller surface of exchange between metal and silicate. We illustrate this point in Fig. 13, for a silicate viscosity of 0.1 Pa.s: the normalized surface of the diapir varies from 1 to 2.3 with decreasing values of R_μ, which means that low R_μ for high *Re* (~100) values lead to an increase of exchange surface by 130% relatively to the initial diapir surface. The same effect is observed for μ_{sil} =1 Pa.s (*Re*~10), to a lesser degree: for low metallic viscosity (R_μ = 0.1) the diapir surface increases by 20%. This leads to an increase in R_c value for all partition coefficients except for $D^{met/sil}$ = 1000, for which an increase in diapir surface has a negligible effect, the deformation occurring over a short timescale at a low reaction rate. This effect is weak in our study compared to the effect of *Re* and $D^{met/sil}$ (see Section 3.4), because the *We* range of our study does not allow major diapir deformation. For the deformation rate to have a strong impact on chemical equilibrium, the *We* values have to be much higher (We> 10, see Lherm & Deguen, 2018).

3.4. Influence of the partition coefficient

We have shown in Figs. 11 and 12 that chemical equilibration was less efficient when the value of the viscosity ratio between the iron and silicate phases was higher. This conclusion also stands for the whole range of partition coefficients used in our models. As detailed in Section 2.2, the higher the value of $D^{met/sil}$, the closer the conditions are to equilibrium conditions, and the lower the reaction rate (R_i) will be. However, the thermodynamical equilibrium is reached faster, which limits the amount of exchange between the metallic droplet and the surrounding silicate. Therefore, the contaminated volume represented by R_C decreases when $D^{met/sil}$ increases (see Figs. 11 and 12). This effect is relatively small: an increase of 3 orders of magnitude decreases *Rc* by less than one order of magnitude.

3.5. Parameterization of the chemical contamination

As shown in the previous sections, the contamination of silicate by a siderophile element depends on the Reynolds number, viscosity ratio, and the values of metal-silicate partition coefficients. To use our results in an iron rain scenario following an impact during planetary formation, it is necessary to quantify the relative effect of each parameter on chemical contamination. In section 3.1 and 3.2 we chose a distance of $10\times R_{Fe}$ and the relevant time (Fig. 5) at which R_C is considered to have reached a stationary value. With

565 this assumption the error is limited, since R_C tends to reach a plateau in all our simulations
566 (see Fig. 8). Therefore, we consider the R_C values obtained from our models at a distance
567 of $10\times R_{Fe}$ in our parameterization.

568 We show in Sections 3.2 and 3.3 that increasing the Reynolds number and viscosity
569 ratio both tend to decrease R_C. In Figs. 11 and 12, $\log(R_c)$ decreases linearly with both
570 $\log(Re)$ and $\log(R_\mu)$ independently of the value of $D^{met/sil}$ with a small error in the prediction
571 ($R^2 > 0.85 - 0.9$). Concerning the effect of partition coefficients, (Section 3.4), all the
572 curves in Figs. 11 and 12 are parallel, showing that there is a linear relationship between
573 $\log(R_c)$ and $\log(D^{met/sil})$. We parameterize the evolution of $\log(R_C)$ as a function of $logRe$,
574 $logR_\mu$ and $logD^{met/sil}$. The method used here is a multi-linear regression fit on all the data
575 retrieved from the simulations:

576 $$logR_C = a\times logD^{met/sil} + b\times logRe + c\times logR_\mu + d \quad (11)$$

577

578 where a, b, c and d are constants fitted to the data by least-square regressions. The values
579 of the parameters are presented in Table 2. As shown in Fig. 14, the parameterization of
580 Eq. (11) shows a relatively good fit to the data retrieved from calculations. This kind of fit
581 is not perfect, and could certainly be improved by including non-linear dependencies. It is
582 also worth noting that this parameterization is valid for a narrow range of Re and We
583 values, and its precision is lower at high Re values (see section 2.4). For instance, different
584 results can be found in turbulent cases (high Re, Deguen et al., 2014) and/or with deformed

585 diapirs (high *We*, Lherm & Deguen, 2018). However, this form of equation (Eq. (11)) is
586 practical to use in models of planetary formation with limited error on the value of R_C,
587 therefore we chose this form to simplify the calculations in sections 5 and 6.

588 This parameterization shows that the main parameters controlling the
589 contamination of a liquid silicate reservoir by a siderophile element during the sinking of
590 a metallic droplet are the Reynolds number and the metal-silicate partition coefficients.
591 The higher the $D^{met/sil}$ is, the less the silicate will be contaminated, which reflects the fact
592 that we consider here a siderophile element. The Reynolds number has the same effect as
593 $D^{met/sil}$: the higher *Re* is, the lower R_C will be. This high absolute value of *b* reflects the
594 importance of the silicate viscosity, which controls the diapir velocity, as well as the type
595 of flow and the deformation of the diapir. The fact that the parameter *b* is negative shows
596 that increasing the value of the Reynolds number will decrease R_C. Indeed, decreasing the
597 viscosity increases the Reynolds number (Eq. 6) as well as the diapir velocity (*e.g.* Samuel,
598 2012; Wacheul et al., 2014, and Fig. 5).

599

600 **4. From a single droplet to the large impact context**

601 In the previous section, we derived a parameterization (Eq. 11) to estimate the volume
602 fraction of a magma ocean contaminated by a unique 1cm-radius metallic droplet. In this
603 section we apply this parameterization to large impacts in the context of late accretion.

604 The parameterization was calculated for a pertinent range of metallic and silicate
605 viscosities. Numerical simulations and laboratory experiments estimated the viscosity of
606 silicate melts at high pressure within the range of 0.01 Pa.s to 1 Pa.s. (Liebske et al., 2005;
607 Karki & Stixrude, 2010; Karki, 2018). This range is stable because the viscosity tends to
608 increase with pressure, but decrease with increasing temperature. As for the viscosity of
609 metallic liquid, few experiments have been made, but the experimental results also show
610 that the range of viscosity for liquid iron alloy is stable, at around 0.01-0.1 Pa.s (Kono et
611 al., 2015). Therefore, the effect of viscosity on the equilibrium rate calculated in our
612 simulation can be extrapolated for a high pressure context in an entirely liquid magma
613 ocean. The higher values (10 -1000 Pa.s) of μ_{sil} tested in our simulation can also be applied
614 at the end of the magma ocean stage when the silicate liquid is starting to crystallize (but
615 before the mushy stage where the flow dynamics is governed by the viscosity of the solid
616 silicate phase).
617 A more limiting factor to the extrapolation of our parameterization to planetary formation
618 is the size of our computational domain. However, it is possible under certain conditions,
619 which are listed below.
620 When a differentiated impactor collides with a growing planet, two fragmentation
621 mechanisms of its metallic core occur. The first fragmentation is induced by the impact
622 itself that stretches and disperses the impactor's core (Kendall and Melosh, 2016). The
623 lunar crater observations showed that the most probable impact angle is $\alpha = 45°$

624 (Shoemaker, 1962). When considering an impactor with a metallic core radius of R_{core}
625 impacting a magma ocean at an angle $\alpha = 45°$, it is possible to apply our parameterization:
626 the dispersion of the impactor's core material becomes the same as our study
627 computational domain. The mantle fraction affected by the impact (i.e. the volume of
628 mantle into which the metallic droplets are initially spread out) can be approximated by
629 the volume of a cylindrical portion with an angle α, a thickness h and a radius L. The
630 volume of mantle affected is then $V_{affected} = \alpha h L^2/2$. For R_{imp}=100 km, R_{core}=50 km,
631 and α=π/4, Kendall & Melosh (2016) give h=200km, L=2000 km: we can then estimate
632 $V_{affected}$ = 3.14 x 10^{17} m^3. After the first fragmentation induced by the impact, a second
633 rapid fragmentation occurs leading to the formation of much smaller droplets of different
634 sizes. Wacheul et al., (2014) showed that metallic diapirs will fragment into droplets with
635 a mean radius of between 4 mm and 20 mm. Assuming an average droplet radius of 1 cm
636 (Rubie et al., 2003) and that all the impactor's core diapir is fragmented into these cm-
637 radius droplets, an impactor's core with radius R_{core}=50 km will fragment into $\approx 10^{20}$ cm-
638 radius droplets. This yields a concentration of 400 droplets/m^3, or 1 droplet per 2.5 liters,
639 which yields a metal/silicate volume ratio of 0.0016 within $V_{affected}$. Currently, no scaling
640 law describes the relation between (L, h, α) and R_{imp} (and as a consequence R_{core}).
641 According to Kendall & Melosh (2016), for R_{core}=50km, $L \approx 40R_{core}$ and $h \approx 4R_{core}$ and by
642 making the assumption that these two relations are also valid for different R_{core} values, we

643 can infer that the ratio of the impactor's core volume over the affected volume is constant
644 for any impactor size.
645
646 In the numerical models described in the previous sections, we consider a metallic droplet
647 sinking into a large volume of molten silicates to avoid boundary effects. In our study the
648 ratio between the volume of the iron droplet and the volume of the computational domain
649 is 0.0019, which is relatively close to the volume ratio of 0.0016 expected after an impact.
650
651 After a large impact, the impactor's core is dispersed within a volume $V_{affected} =$
652 $\alpha h L^2/2$. Assuming the formation of a cloud of cm-radius droplets with an iron fraction
653 $\chi_{Fe} = 0.0016$ within $V_{affected}$, the volume where chemical exchange between the
654 droplets and the magma ocean will occur is:
655
656 $$V_{exch} = R_c V_{affected} \quad (12)$$
657
658 Using Eq. (11), Tab. 2 and considering L=40R_{core} and h = 4R_{core} (Kendall and Melosh,
659 2016), we can calculate the fraction of the volume of the Earth's mantle V_{exch}/V_{mantle} in
660 which chemical exchange is likely to occur. Fig. 15 shows V_{exch}/V_{mantle} as a function of the
661 impactor radius and illustrates the influence of the partition coefficient and the viscosity
662 contrast between the magma ocean and the liquid iron on this ratio.

As the impactor size increases, the mantle volume chemically affected by the impact increases by R_{imp}^3. This relation is constrained by the simple formula we have used to relate $V_{affected}$ to R_{core}. Given the current knowledge of the impact-induced fragmentation mechanisms of an iron core on a planetary scale, this simplification is a first step toward a global understanding of the chemical equilibration occurring after a large impact. Fig. 15 (left) illustrates that an increase in partition coefficient leads to a decrease in the ratio V_{exch}/V_{mantle} in agreement with Eq. (11) and the values from Tab. 2. Fig. 15 (left) shows that for R_{core}=1000 km, increasing the partition coefficient by 2 orders of magnitude decreases the value of the ratio V_{exch}/V_{mantle} by a factor of 3. This effect is significant but less important than the influence of the viscosity ratio. Fig. 15 (right) shows that increasing the magma ocean viscosity relative to a constant liquid iron viscosity of 0.1 Pa.s from 0.1 Pa.s to 100 Pa.s leads to an increase in V_{exch}/V_{mantle} by a factor of more than 5. According to Fig. 15, a very large impact such as that which led to the formation of the Moon-Earth system, involving a highly viscous magma ocean, would strongly enhance the chemical equilibration between the impactor's core and the Earth's mantle. This result needs to be nuanced, since a large impact is likely to increase temperature and therefore lower the viscosity of the magma ocean.

5. Signature of a large impact on the mantle composition

This section aims at improving previous accretion models (e.g. Fischer et al., 2015, Siebert et al., 2012, Wood et al., 2008) by accounting for a possible chemical disequilibrium at a given depth. Previous models assumed that at a given step in accretion, equilibrium is reached throughout the entire mantle (Wood et al., 2008; Siebert et al., 2012; Boujibar et al., 2014; Clesi et al., 2016). This equilibrium is set by the final pressure on reaching equilibrium, usually at a depth corresponding to 50 % of the core mantle boundary depth (or close to this depth, for instance in Rubie et al., 2015), in order to fit the Ni and Co partitioning behavior (Bouhifd & Jephcoat, 2003;2011; Fischer et al., 2015).

In this section and the following one, the hypothesis is the same as in previous models of accretion, but with the notable exception that not all of the mantle reaches equilibrium. The amount of mantle equilibrated is defined using Eqs. (11) and (12), i.e. our parameterization is applied directly to a classical model of equilibration in a magma ocean, thus adding one step of complexity to previous models.

5.1. Geochemical elements of interest

To estimate the chemical equilibrium between the impactor's core and the impacted mantle, we focus our calculations on the chemical behavior of moderately siderophile elements such as Ni and Co for which $D^{met/sil}$ is strongly dependent on pressure (Bouhifd & Jephcoat, 2003, 2011; Siebert et al., 2012; Fischer et al., 2015). These two elements are important, since the models of deep magma ocean are designed to explain their relatively high abundances in the BSE (Drake and Righter, 2002). The maximum depth of the

magma ocean (around 50% the CMB depth throughout accretion) is derived from the pressure for which the partitioning behavior of Ni and Co yields a 19.05±2 ratio in the BSE (Bouhifd & Jephcoat, 2003, 2011). In the previous sections, we considered a generic, moderately siderophile element with a metal/silicate partition coefficient ranging from 1 to 1000. This range is large enough to extrapolate the trend derived from our simulations to the behavior of Ni and Co at high pressure. For Ni, this partition coefficient ranges between ≈400 for P =1 GPa, and ≈ 20 for 40<P<60 GPa. For Co, the partition coefficient ranges between ≈ 100 for P = 1 GPa and ≈ 20, for 40<P<60 GPa (Bouhifd & Jephcoat, 2011 and references therein). In the models presented below, we assume that the pressure of equilibrium after an impact corresponds to the last stages of equilibrium in a deep magma ocean, at between 50 and 60 GPa (see Appendix B in Clesi et al., 2016 for the corresponding calculations and the full evolution of pressure, temperature and f_{O2} during the accretion) with values of Ni and Co partition coefficients of between 20 and 80 for the corresponding f_{O2}. In the following section, we consider that the iron content of the mantle is close to the BSE content (8% wt) and is not affected by the impact. The f_{O2} is then considered constant relatively to the iron-wüstite buffer and its value is $\log f_{O2} \approx -2$ ΔIW. In this case, the Ni and Co partition coefficients have converged toward the same value: $D^{met/sil} \approx 20$, which is used in the following calculations.

5.2. Chemical signature of a large impact on the Ni/Co ratio

Here we characterize the effect of a single impactor on the Ni/Co ratio in the mantle. We consider an initially fully accreted Earth. The reference composition of the impacted mantle is set to the BSE composition defined in McDonough and Sun, (1995) (Ni/Co = 19.05, 2000 ppm of Ni and 105 ppm of Co in the mantle). We consider that the silicate fraction of the impactor is lost during impact and that only its metallic core is trapped within the impacted mantle. The impactor has a radius of between 10 km and 1000 km and the same composition as the Earth's core (McDonough, 2003). Given the range of impactor size, the mass accreted is negligible compared to the Earth's mass: with a mean density of 9400 $kg.m^{-3}$, a metallic impactor of 1000 km radius adds a total mass of $\sim 3.10^{22}$ kg, which is 0.5% of the Earth's mass. This choice of size and composition for the impactor allows us to focus on the change in mantle concentration, without changing the final core concentration, especially the light element (Si and S) content, in the core. Furthermore, this impactor composition, and its relatively low mass, would not significantly change the oxygen fugacity and thus does not affect the partitioning behavior of Ni and Co.

This section aims at characterizing the partitioning behavior of Ni and Co as a function of the impactor radius and the viscosity contrast R_μ computing Eqs. (11) and (12). The first term of Eq. (11) illustrates the influence of the partition coefficients for Ni and Co. These

743 partition coefficients are controlled mainly by pressure and temperature, as well as the
744 composition of the metallic phase, and oxygen fugacity (Bouhifd & Jephcoat, 2003, 2011,
745 Siebert et al., 2012, Fischer et al., 2015). To obtain partitioning behavior independent of
746 oxygen fugacity, we use the exchange partition coefficient K_d, which is the
747 thermodynamical constant of the reaction:

748 $$MO_{n/2} + \frac{n}{2}Fe \rightarrow \frac{n}{2}FeO + M \qquad (13)$$

749 Where M is the element considered (in our case Ni or Co), and n is the valence of the
750 element M (in our case, n= 2). In reaction (13), the oxides are in the silicate phase, while
751 the reduced element is in the metallic phase. The exchange partition coefficient is given
752 by $K_d = \frac{c_M}{c_{MO_{n/2}}} \times \left(\frac{c_{FeO}}{c_{Fe}}\right)^{n/2}$ where c_M and c_{Fe} are the molar fractions of M and Fe in the
753 metallic phase, and c_{FeO} and $c_{MO_{n/2}}$ are the molar fractions of FeO and $MO_{n/2}$ in the
754 silicate phase. To estimate the values of the partition coefficients, we use the
755 parameterization of K_d from Clesi et al., (2016), where we ignore the effect of water, as
756 well as the carbon content in the metallic phase. The exchange partition coefficient, K_d, is
757 given by:
758
759 $$logK_d^{element} = \frac{b_{el}}{T} + c_{el}\frac{P}{T} + e_{el}log\left(1 - \chi_{Si}^{metal}\right) + g_{el}log\left(1 - \chi_S^{metal}\right) + h_{el}$$
760 (14)
761

762 The parameters b_{el}, c_{el}, e_{el}, g_{el} and h_{el} are detailed in Clesi et al., (2016), and are different
763 for each element studied. *P* and *T* are the pressure (in GPa) and temperature (in Kelvin)
764 of equilibrium, respectively, corresponding to the pressure at 50% of CMB depth (i.e.,
765 1450 km), and the liquidus temperature associated with it (Andrault et al., 2011). We
766 assume here an equilibrium pressure of 63 GPa, and an equilibrium temperature of 3450
767 K. χ_{Si}^{metal} and χ_{S}^{metal} are the mass fractions of silicon and sulfur in the impactor. We
768 assume here that χ_{Si}^{metal} =0.06 and χ_{S}^{metal} =0.019 (McDonough, 2003). K_d is then
769 converted into a Nernst partition coefficient (mass ratio) following:
770
771 $$D^{met/sil} = \frac{M_{oxide} \times M_{Fe}}{M_{FeO} \times M_{element}} \times K_d^{element} \times D_{Fe}^{met/sil} \quad (15)$$
772
773 where $M_{element}$ is the molar mass of Ni or Co, M_{oxide} is the molar mass of NiO or CoO, and
774 M_{Fe} and M_{FeO} are the molar masses of Fe and FeO respectively. $D_{Fe}^{met/sil}$ is the partition
775 coefficient of iron and equals 13.65 in the BSE model. We consider that the impactor does
776 not significantly change the oxygen fugacity and therefore does not influence the $D_{Fe}^{met/sil}$
777 value.
778 The second term in Eq. (11) characterizes the influence of the Reynolds number, which is
779 given by Eq. (6). As stated in Section 4, we consider that the metal fragments into droplets
780 with a radius of 1 cm. The sinking velocity of these droplets is given by Eq. (9). We
781 assume here a silicate density of ρ_{mantle} =4500 kg.m^{-3} (mean density of the Earth's mantle),

782 a metallic density of ρ_{metal}= 9400 kg.m^{-3}, which is consistent with iron rich liquid alloys
783 at these pressures (Morard et al., 2013) and the current Earth's value for the acceleration
784 of gravity (i.e., 9.81 m.s^{-2}). The viscosity of the silicate phase in our calculations ranges
785 from 0.1 to 100 Pa.s. The third term in Eq. (11) measures the influence of the viscosity
786 ratio $R_\mu = \mu_{met}/\mu_{sil}$. In our calculations, we consider a constant value for the metallic
787 viscosity (= 0.1 Pa.s), consistent with iron liquid viscosity at high pressure (Kono et al.,
788 2015).
789
790 Once the parameter *Rc* is calculated for Ni and Co, the impactor equilibrates with a volume
791 of mantle defined by Eq. (12) in section 4, considering that $V_{impactor}/V_{affected}$ = 0.0016,
792 independent of the size of the impactor. As R_C expresses the volume fraction of the silicate
793 that has reacted with the metal, it may overestimate the volume of the mantle that has
794 equilibrated with the metal phase. Hence the parameter R_C should be considered as a first-
795 order approximation of the volume equilibrated. Therefore, for Eq. (12), the mass of
796 mantle that is equilibrated is obtained by simple multiplication by ρ_{mantle}. In this mass of
797 mantle, the concentration of Ni or Co is in equilibrium and is given by $\chi_{eq}^{silicate} =$
798 $\frac{\chi_{impactor}^{metal}}{D^{met/sil}}$. The final mass fraction of Ni or Co is given by:
799
800 $$\chi_{final}^{silicate} = \chi_{initial}^{silicate} + (\chi_{eq}^{silicate} - \chi_{initial}^{silicate}) \frac{m_{equilibrated}}{m_{mantle}} \quad (16)$$
801

where, $\chi_{final}^{silicate}$ is the concentration of Ni or Co in the final mantle, $\chi_{initial}^{silicate}$ is the initial concentration of Ni or Co in the mantle, $\chi_{eq}^{silicate}$ is the concentration at equilibrium, $m_{equilibrated}$ is the mass that is equilibrated and m_{mantle} is the mass of the Earth's mantle. The final Ni/Co ratio is then derived from $\chi_{final}^{silicate}$ for Ni and Co. The results of calculations for different viscosities as a function of the impactor radius are presented in Fig. 16.

Fig. 16 shows that a single impactor, even a large one, does not significantly affect the Ni/Co ratio in the mantle. The maximum variation is 0.25 %, and is obtained for a large impactor (1000 km radius) for a relatively high viscosity of the magma ocean (100 Pa.s). For low viscosities (0.1 and 1 Pa.s), a metallic impactor weakly affects the Ni/Co ratio in the mantle (less than 0.1 % change for a 1000 km radius impactor). Such a small variation confirms that high spatial resolution models are not necessary even for large Pe_{mesh} values obtained for low viscosities. For a relative error of 100% in the values of R_c , at a viscosity of 0.1 Pa.s, it would only induce a variation in Ni/Co of between 0 and 0.2% within the final model.

Eq. (16) shows that the final concentration is proportional to the volume equilibrated if $\chi_{eq}^{silicate}$ is higher than $\chi_{initial}^{silicate}$. In this case, late accretion of a metallic impactor, which yields a high metallic concentration in Ni and Co (similar to the Earth core concentration given in McDonough, 2003); with a high equilibrium pressure, which yields low partition coefficient values for Ni and Co, $(\chi_{eq}^{silicate} - \chi_{initial}^{silicate})$ is positive. The impactor is

metallic and rich in Ni and Co (5.2%wt and 0.24 %wt, respectively), and impacts a silicate mantle with a BSE composition. Therefore, when the mass of mantle equilibrated is higher, the variation in Ni or Co concentration compared to the BSE in the mantle is higher. If the disequilibrium is high, the $m_{equilibrated}$ is low, and therefore there is less variation in the Ni/Co ratio. As shown in Fig. 16, the amount of disequilibrium is higher for a low viscosity magma ocean, as well as for small metallic impactors, and therefore there is no change in the moderately siderophile element concentrations in the mantle under these conditions. This means that, to have a significant effect on the moderately siderophile element concentrations in the BSE, late accretion impactors need to be large and impact a viscous magma ocean in order to increase the degree of equilibrium. Even in this case, if the amount of Ni and Co in the impactor is not significantly higher than that in the Earth's core, the change in BSE composition will not be significant, as illustrated in Fig. 16.

6. Discussion

6.1. Earth accretion models and magma ocean properties

In the previous section we characterized the effects of a late impact, negligible in mass, composed only of a metallic phase. However, most of the disequilibrium happens during accretion. Therefore, Eq. (16) is not relevant, at least not in this form, in the context of a growing planet. Assuming that the mantle of the impactor and of the growing Earth is well

mixed before equilibration with the metallic fraction, we can define the concentration of the post-impact mantle, $\chi^{silicate}_{post-impact}$. By modifying Eq. (16), and knowing the composition of the impactor's metallic phase it is possible to calculate the composition of a growing planetary mantle before it equilibrates with the metallic phase of the impactor. It is given by:

$$\chi^{silicate}_{post-impact} = \frac{m_{mantle}}{m_{mantle}-m_{equilibrated}}\left(\chi^{silicate}_{final} - \frac{m_{equilibrated}}{m_{mantle}}\chi^{silicate}_{equilbrated}\right) \quad (17)$$

Since $m_{equilibrated}$ is dependent on the size of the impactor core and magma ocean viscosity, it is possible to calculate the composition of the mantle for a 90% accreted Earth hit by a Mars-sized impactor (Moon-forming impact) as a function of the impactor's core radius and viscosity of the magma ocean. Fig. 17 shows the corresponding results for comparison with Fig. 16: in this case, the greater the degree of equilibrium, the lower the initial Ni/Co ratio.

The results displayed in Fig. 17 show that it is possible to reach the same final Ni/Co ratio for the Earth's mantle with drastically different properties of the impactor and the magma ocean. From Fig. 17, two post-impact models can be derived:

- A model with a low $R_{core}/R_{impactor}$ ratio and low magma ocean viscosity, which yields a lower degree of equilibrium between metal and silicate. In this kind of model, the composition of the Earth's mantle is more dependent on the equilibrium conditions between the metallic phase and the silicate phase than on

the composition of the impactor. For instance, the models presented in *e.g.* Burbine & O'Brien (2004), Rai & van Westrenen (2013) or Dauphas et al., (2014) are based on mixing different chondritic compositions where the main parameter fitted is the isotopic consistency, and they are therefore predominantly compositionally-derived models. For these models to be consistent, the impactor's core needs to be small ($R_{core}/R_{impactor}$ < 0.4, left-hand side of Fig. 17), and the magma ocean viscosity low ($\mu_{magma\ ocean} \approx$ 0.1- 1 Pa.s), so as to achieve a low equilibrium rate between metal and silicate.

- A model with a high $R_{core}/R_{impactor}$ ratio, and high viscosity of the magma ocean, which yields greater equilibrium between metal and silicate. In this kind of model, the main changes in Earth mantle composition are due more to the composition of the impactor and less to the chemical reactions between metal and silicate. For instance, the models presented in *e.g.* Wood et al., 2008, Siebert et al., 2012 and Boujibar et al., 2014 are based on the metal-silicate partitioning behavior, where the discriminating parameter is the relative core/mantle abundances of siderophile elements, and they are therefore predominantly equilibrium-derived models. In this kind of model, a minimal equilibrium needs to be reached, and therefore the impactor's core needs to be large ($R_{core}/R_{impactor}$ > 0.4, right-hand side of Fig. 17), and/or the magma ocean viscosity needs to be high ($\mu_{magma\ ocean} \approx$ 10-100 Pa.s).

To summarize, our results cannot constrain the viscosity of the magma ocean (especially given the error in our calculations for low viscosity calculations, see Section 2.4), but for a given model, our results can constrain the range of magma ocean viscosities in order to reach the BSE concentrations for moderately siderophile elements.

However, this work needs to be done for each accretion step or impact, and for each element, which would increase the number of plausible scenarios to accrete the Earth, but could also provide compositional constraints on irreconcilable scenarios, and therefore allow some impactor compositions to be excluded from a given model.

6.2. Effect of Moon formation on the Ni/Co ratio in the Earth's mantle

In the previous section we showed that the properties of the magma ocean are model dependent: they have to be inferred from the impactor properties and the final BSE content chosen as a control of the model output. In this section, we infer the viscosity of a magma ocean for one particular model: the Moon formation by an impact with a Mars-sized impactor (Canup, 2004). The Moon forming impactor (named Theia) is believed to be a large Mars-sized impactor which hit the proto-Earth at the end of accretion with an oblique trajectory (Canup & Asphaug, 2001, Canup, 2004). In a simulation of this kind of impact, most of the metal and silicate of the impactor merges with the Earth (Canup, 2004). If we consider mass of the Moon to be negligible compared to that of Theia, and ignore the loss of particles due to the impact, we can determine that the final 10% mass accreted to the

902 Earth was due to the impact with Theia. The core of this impactor is 30% of the total mass
903 of the impactor (Canup, 2004), with the same mean density as the Earth, so it is not
904 improbable that the ratio $R_{core}/R_{impactor}$ is comparable to that of the Earth or Mars today
905 (given by the red and blue vertical lines in Figs. 17). In that case, Eq. (17) and Fig. 17
906 shows that some equilibrium occurred between the magma ocean formed by the impact
907 and the impactor's core sinking into the Earth's core. For every magma ocean viscosity
908 tested here, it is necessary to have interaction between Theia's core and the proto-Earth's
909 mantle to get the final BSE concentration. For a magma ocean viscosity of 0.1 Pa.s, the
910 proto-Earth's Ni/Co ratio is between 0.25 % and 0.45 % lower than the BSE values for a
911 $R_{core}/R_{impactor}$ comparable to those of Mars and the Earth respectively. For a magma ocean
912 viscosity of 100 Pa.s, the proto-Earth Ni/Co ratio is between 1.45% and 3.00 % lower than
913 the BSE values for a $R_{core}/R_{impactor}$ comparable to those of Mars and the Earth, respectively.
914 This means that the Moon forming impact had a significant effect on the BSE Ni/Co ratio,
915 which can be high if the magma ocean formed after the impact was viscous (100 Pa.s) and
916 the core radius of Theia was around 1850 km.
917
918
919 **7. Conclusion**

920 We developed numerical models to characterize the effects of viscosity and partition
921 coefficients on the metal/silicate equilibrium for moderately siderophile elements. We

922 showed that the volume of silicate equilibrated with a small volume of metal is mostly
923 controlled by the partition coefficients and the viscosity of the silicate. The viscosity ratio
924 between metal and silicate is a second order parameter but still has a significant effect.
925 The scope of this study does not include other elements that have different partitioning
926 behavior (V, Cr, Mn etc.) and future models of equilibrium between metal and silicate
927 will have to integrate these elements to get a clearer view of chemical exchanges within
928 the Early Earth. Furthermore, the range of *Re* and *We* covered in this study does not cover
929 the whole range of *Re* and *We* numbers during the accretion event (Fig. 10). Therefore, in
930 the future, we will need to model more complex flows (such as shown in Samuel, 2012 or
931 Wacheul et al., 2014), to widen the scope of our interpretations (see Section 4 for the
932 extrapolation conditions). Future models should also account for the thermal equilibration
933 during metal/silicate separation (Wacheul & Le Bars, 2018) to characterize the effects of
934 temperature on the partition coefficient values. Other phenomena, while important**,** are
935 ignored due to being beyond the scope of the study, for instance the effect of the droplet
936 size and shape (Qaddah et al., 2019), or stretch-enhancing diffusion (Lherm & Deguen,
937 2018), or the possibility of large core-merging events (Landeau et al., 2016). All these
938 phenomena are beyond the scope of this study and should be taken into account in further
939 work and models of accretion.
940 Nevertheless, we proposed a parameterization of the disequilibrium between a silicate
941 magma ocean and a metallic droplet for moderately siderophile element behavior. Using

this parameterization on Ni and Co behavior at the end of accretion, it is possible to define some constraints on the viscosity of the magma ocean. For a given model of accretion to fit the current BSE concentrations, the viscosity of the magma ocean and the impactor composition need to be changed accordingly: large impactors with large metallic cores (R_{core} > 1100 km) and high magma ocean viscosity (10 -100 Pa.s) favor a high degree of metal/silicate equilibrium; while metal/silicate disequilibrium models can be achieved with moderately small metallic cores (R_{core} ≈ 300-1000 km) and low viscosity (0.1 - 1 Pa.s) magma ocean.

When applying our results to the Moon-forming impact, we showed that the current Ni/Co ratio in the BSE is affected by the Moon's formation, depending on the viscosity of the magma ocean formed after the impact. The Moon's formation can account for 0.25 to 0.45 % of the final BSE Ni/Co ratio for a low viscosity (0.1 Pa.s) magma ocean, and for 1.45% to 3 % of the final BSE Ni/Co ratio for a high viscosity (100 Pa.s) magma ocean.

Acknowledgments

This research received funding from the French PNP program (INSU-CNRS), the French Government Laboratory of Excellence initiative No. ANR-10-LABX- 0006 and the Région Auvergne. This paper is Laboratory of Excellence ClerVolc contribution No. **xxx**. This project has received funding from the European Research Council (ERC) under the European Union's Horizon 2020 research and innovation programme (grant agreement 681835 FLUDYCO-ERC-2015-CoG). This project has received funding from the European Research Council (ERC) under the European Union's Horizon 2020 research and innovation programme (grant agreement 716429). We thank Renaud Deguen for his fruitful comments.

References

C. J. Allegre, J.-P. Poirier, E. Humler, and A. W. Hofmann. The Chemical composition of the Earth. *Earth and Planetary Science Letters*, 134:515–526, 1995.

D. Andrault, N. Bolfan-Casanova, G. Lo Nigro, M. A. Bouhifd, G. Garbarino and M. Mezouar. Solidus and liquidus profiles of chondritic mantle: Implication for melting of

the Earth across its history. *Earth and planetary science letters*, 304(1-2):251-259, 2011.

M. A. Bouhifd and A.P. Jephcoat. Convergence of Ni and Co metal-silicate partition coefficients in the deep magma-ocean and coupled silicon-oxygen solubility in iron melts at high pressures. *Earth and Planetary Science Letters*, 307(3-4):341–348, 2011.

M. A. Bouhifd and A.P Jephcoat. The effect of pressure on partitioning of Ni and Co between silicate and iron-rich metal liquids: a diamond-anvil cell study. *Earth and Planetary Science Letters*, 209(1-2):245–255, 2003.

M.A. Bouhifd, V. Clesi, A. Boujibar, N. Bolfan-Casanova, C. Cartier, T. Hammouda, M. Boyet, G. Manthilake, J. Monteux and D. Andrault. Silicate melts during Earth's core formation. *Chemical Geology*, 461, 128-139, 2017.

A. Boujibar, D. Andrault, M. A. Bouhifd, N. Bolfan-Casanova, J.-L. Devidal, and N. Trcera. Metal-silicate partitioning of sulphur, new experimental and thermodynamic constraints on planetary accretion. *Earth and Planetary Science Letters*, 391:42– 54, 2014.

994 T.H. Burbine, and K.M. O'Brien. Determining the possible building blocks of the Earth
995 and Mars. *Meteoritics & Planetary Science*, 39(5):667-681, 2004.
996
997 C. Cartier, T. Hammouda, M. Boyet, M. A. Bouhifd and J.-L. Devidal. Redox control
998 of the fractionation of niobium and tantalum during planetary accretion and core
999 formation. *Nature Geoscience*, 7(8):573, 2014
1000
1001 R.M. Canup. Simulations of a late lunar-forming impact. *Icarus*, 168(2):433–456,
1002 2004.
1003
1004 R. M. Canup. Accretion of the Earth. *Philosophical Transactions of the Royal Society*
1005 *A: Mathematical, Physical and Engineering Sciences*, 366(1883):4061-4075, 2008.
1006
1007 R. M. Canup, and E. Asphaug. Origin of the Moon in a giant impact near the end of the
1008 Earth's formation. *Nature*, 412(6848):708, 2001.
1009
1010 I. D. Chang.On the wall effect correction of the Stokes drag formula for axially
1011 symmetric bodies moving inside a cylindrical tube. *Zeitschrift für angewandte*
1012 *Mathematik und Physik ZAMP*, 12(1):6-14, 1961.

1013 V. Clesi, M.A. Bouhifd, N. Bolfan-Casanova, G. Manthilake, A. Fabbrizio, and D.
1014 Andrault. Effect of H2O on metal-silicate partitioning of Ni, Co, V, Cr, Mn and Fe:
1015 Implications for the oxidation state of the Earth and Mars. *Geochimica et*
1016 *Cosmochimica Acta*, 192:97–121, 2016.
1017
1018 J. Crank. *The Mathematics of Diffusion*, 2nd ed. Clarendon Press, Oxford. viii, 414 p,
1019 1975.
1020
1021 T. W. Dahl and D. J. Stevenson. Turbulent mixing of metal and silicate during planet
1022 accretion and interpretation of the Hf-W chronometer. *Earth and Planetary Science*
1023 *Letters*, 295(1-2):177–186, 2010.
1024
1025 N. Dauphas, J. H. Chen, J. Zhang, D. A. Papanastassiou, A. M. Davis, and C.
1026 Travaglio. Calcium-48 isotopic anomalies in bulk chondrites and achondrites: Evidence
1027 for a uniform isotopic reservoir in the inner protoplanetary disk. *Earth and Planetary*
1028 *Science Letters*, 407:96-108, 2014.
1029
1030 R. Deguen, P.Olson, and P. Cardin. Experiments on turbulent metal-silicate mixing in a
1031 magma ocean. *Earth and Planetary Science Letters*, 310(3-4):303–313, 2011
1032

1033 R. Deguen, M. Landeau, and P.Olson. Turbulent metal-silicate mixing, fragmentation,
1034 and equilibration in magma oceans. *Earth and Planetary Science Letters*, 391:274–287,
1035 2014.
1036
1037 M. J. Drake, and K. Righter. Determining the composition of the Earth. *Nature*,
1038 416(6876):39, 2002.
1039
1040 R. A. Fischer, Y. Nakajima, A. J. Campbell, D. J. Frost, D. Harries, F. Langenhorst, N.
1041 Miyajima, K. Pollok, and D. C. Rubie. High pressure metal-silicate partitioning of Ni,
1042 Co, V, Cr, Si, and O. *Geochimica et Cosmochimica Acta*, 167:177–194, 2015.
1043
1044 J. R. Fleck, C. L. Rains, D. S. Weeraratne, C. T. Nguyen, D. M. Brand, S. M Klein, J.
1045 M. McGehee, J. M. Rincon, C. Martinez and P.L Olson. Iron diapirs entrain silicates to
1046 the core and initiate thermochemical plumes. *Nature communications*, *9*(1), 71, 2018.
1047
1048 B. Jacobsen, Q.- Z. Yin, F. Moynier, Y.Amelin, A. N. Krot, K. Nagashima, I. D.
1049 Hutcheon, and H. Palme. 26Al-26Mg and 207Pb-206Pb systematics of Allende CAIs:
1050 Canonical solar initial 26Al/27Al ratio reinstated. *Earth and Planetary Science Letters*,
1051 272(1-2):353–364, 2008.
1052

1053 J. H. Jones and M. J. Drake. Geochemical constraints on core formation in the Earth.
1054 *Nature*, 322(6076):221, 1986.
1055
1056 B. B., Karki, D. B., Ghosh, and S. K. Bajgain. Simulation of Silicate Melts Under
1057 Pressure. In *Magmas Under Pressure* : 419-453, 2018
1058
1059 B; B. Karki. and L. P. Stixrude. Viscosity of MgSiO3 liquid at Earth's mantle
1060 conditions: Implications for an early magma ocean. *Science*, 328(5979):740-742, 2010.
1061
1062 Y. Ke and Solomatov, V. S. Coupled core-mantle thermal evolution of early Mars.
1063 *Journal of Geophysical Research: Planets*, 114(E7), 2009
1064
1065 J. D. Kendall and H. J. Melosh. Differentiated planetesimal impacts into a terrestrial
1066 magma ocean: fate of the iron core. *Earth and Planetary Science Letters*, 448:24–33,
1067 2016.
1068
1069 T. Kleine, C. Munker, K. Mezger, and H. Palme. Rapid accretion and early core
1070 formation on asteroids and the terrestrial planets from Hf-W chronometry. *Nature*,
1071 418(6901):952–955, 2002.
1072

T. Kleine, M. Touboul, B. Bourdon, F. Nimmo, K. Mezger, H. Palme, S.B. Jacobsen, Q.-Z. Yin, and A.N. Halliday. Hf–W chronology of the accretion and early evolution of asteroids and terrestrial planets. *Geochimica et Cosmochimica Acta*, 73(17):5150–5188, 2009.

T. Kleine and J. F. Rudge. Chronometry of meteorites and the formation of the Earth and Moon. *Elements*, 7(1):41–46, 2011.

Y. Kono, C. Kenney-Benson, Y. Shibazaki, C. Park, G. Shen, and Y.Wang. High-pressure viscosity of liquid Fe and FeS revisited by falling sphere viscometry using ultrafast X-ray imaging. *Physics of the Earth and Planetary Interiors*, 241:57–64, 2015.

M. Landeau, P. Olson, R. Deguen and B. H. Hirsh. Core merging and stratification following giant impact. *Nature Geoscience*, 9(10):786, 2016.

V. Lherm and R. Deguen. Small-Scale Metal/Silicate Equilibration During Core Formation: The Influence of Stretching Enhanced Diffusion on Mixing. *Journal of Geophysical Research: Solid Earth*, 123(12):10,496-10,516, 2018.

C. Liebske, B. Schmickler, H. Terasaki, B. T. Poe, A. Suzuki, K. I. Funakoshi, K.i. Funakochi, R. Ando and D. C. Rubie. Viscosity of peridotite liquid up to 13 GPa: Implications for magma ocean viscosities. *Earth and Planetary Science Letters*, 240(3-4):589-604, 2005.

U. Mann, D. J. Frost and D. C. Rubie. Evidence for high-pressure core-mantle differentiation from the metal–silicate partitioning of lithophile and weakly-siderophile elements. *Geochimica et Cosmochimica Acta*, 73(24):7360-7386, 2009.

W. F. McDonough. 3.16–Compositional model for the Earth's core. *Treatise on geochemistry*, :547-568, 2003.

W. F. McDonough and S.-S. Sun. The composition of the Earth. *Chemical Geology*, (120): 223–253, 1995.

R. C. Mittal and R. K. Jain. Redefined cubic B-splines collocation method for solving convection–diffusion equations. *Applied Mathematical Modelling*, 36(11)): 5555-5573, 2012.

1111 J. Monteux, Y. Ricard, N. Coltice, F. Dubuffet and M. Ulvrova. A model of metal–
1112 silicate separation on growing planets. *Earth and Planetary Science Letters*, *287*(3-
1113 4):353-362, 2009.
1114
1115 J. Monteux, H. Amit, G. Choblet, B. Langlais and G. Tobie. Giant impacts,
1116 heterogeneous mantle heating and a past hemispheric dynamo on Mars. *Physics of the*
1117 *Earth and Planetary Interiors*, 240:114-124, 2015.
1118
1119 G. Morard, J. Siebert, D. Andrault, N. Guignot, G. Garbarino, F. Guyot, F. and D.
1120 Antonangeli. The Earth's core composition from high pressure density measurements of
1121 liquid iron alloys. *Earth and Planetary Science Letters*, 373:169-178, 2013.
1122
1123 M. Nakajima and D. J. Stevenson. Melting and mixing states of the Earth's mantle after
1124 the Moon-forming impact. *Earth and Planetary Science Letters*, 427:286-295, 2015
1125
1126 D. P. O'Brien, A. Morbidelli and H.F. Levison. Terrestrial planet formation with strong
1127 dynamical friction. *Icarus*, 184(1):39-58, 2006.
1128
1129 E. Olsson, and G. Kreiss. A conservative level set method for two phase flow. *Journal*
1130 *of computational physics*, 210(1):225-246, 2005.

B. Qaddah, J. Monteux, V. Clesi, M. A. Bouhifd and M. Le Bars. Dynamics and stability of an iron drop falling in a magma ocean. *Physics of the Earth and Planetary Interiors*, 289:75-89, 2019.

B. Qaddah, J. Monteux and M. Le Bars. Thermal evolution of a metal drop falling in a less dense, more viscous fluid. *Physical Review Fluids*, 5(5): 053801, 2020.

N. Rai, and W. van Westrenen. Core-mantle differentiation in Mars. *Journal of Geophysical Research: Planets*, 118(6):1195-1203, 2013.

Y. Ricard, O. Šrámek, and F. Dubuffet. A multi-phase model of runaway core-mantle's segregation in planetary embryos. *Earth and Planetary Science Letters*, 284(1-2):144–150, 2009.

K. Righter. Prediction of metal-silicate partition coefficients for siderophile elements: An update and assessment of P-T conditions for metal-silicate equilibrium during accretion of the Earth. *Earth and Planetary Science Letters*, 304(1-2):158–167, 2011.

1150 D. C. Rubie, D.J. Frost, U. Mann, Y. Asahara, F. Nimmo, K. Tsuno, P. Kegler, A.
1151 Holzheid, and H. Palme. Heterogeneous accretion, composition and core-mantle
1152 differentiation of the Earth. *Earth and Planetary Science Letters*, 301(1-2):31–42,
1153 2011.
1154
1155 D.C. Rubie, H.J. Melosh, J.E. Reid, C. Liebske, and K. Righter. Mechanisms of metal-
1156 silicate equilibration in the terrestrial magma ocean. *Earth and Planetary Science*
1157 *Letters*, 205(3-4): 239–255, 2003.
1158
1159 D.C. Rubie, S.A. Jacobson, A. Morbidelli, D.P. O'Brien, E.D. Young, J. de Vries, F.
1160 Nimmo, H. Palme, and D.J. Frost. Accretion and differentiation of the terrestrial planets
1161 with implications for the compositions of early-formed Solar System bodies and
1162 accretion of water. *Icarus*, 248:89–108, 2015.
1163
1164 J. F. Rudge, T. Kleine, and B. Bourdon. Broad bounds on Earth's accretion and core
1165 formation constrained by geochemical models. *Nature Geoscience*, 3(6):439–443,
1166 2010.
1167
1168 H. Samuel and P. J. Tackley. Dynamics of core formation and equilibration by negative
1169 diapirism. *Geochemistry, Geophysics, Geosystems*, 9(6), 2008.

H. Samuel. A re-evaluation of metal diapir breakup and equilibration in terrestrial magma oceans. *Earth and Planetary Science Letters*, 313-314:105–114, 2012.

E. M. Shoemaker. Interpretation of lunar craters. *Physics and Astronomy of the Moon* : 283-359, 1962

J. Siebert, J. Badro, D. Antonangeli, and F. J. Ryerson. Metal-silicate partitioning of Ni and Co in a deep magma ocean. *Earth and Planetary Science Letters*, 321-322:189–197, 2012.

D.J. Stevenson. Models of the Earth's core. *Science*, 214(4521):611–619, 1981.

M. Ulvrová, N. Coltice, Y. Ricard, S. Labrosse, F. Dubuffet, J. Velímský, and O. Šrámek. Compositional and thermal equilibration of particles, drops, and diapirs in geophysical flows. *Geochemistry, Geophysics, Geosystems*, 12(10), 2011.

O. Šrámek., Y. Ricard, and F. Dubuffet. A multiphase model of core formation. *Geophysical Journal International*, 181(1):198–220, 2010.

1189 J.-B. Wacheul and M. Le Bars. Fall and fragmentation of liquid metal in a viscous
1190 fluid. *Physical Review Fluids*, 2(9):090507, 2017.
1191
1192 J.-B. Wacheul and M. Le Bars. Experiments on fragmentation and thermo-chemical
1193 exchanges during planetary core formation. *Physics of the Earth and Planetary*
1194 *Interiors*, 276:134-144, 2018.
1195
1196 J-B-Wacheul, M. Le Bars, J. Monteux, and J. M. Aurnou. Laboratory experiments on
1197 the breakup of liquid metal diapirs. *Earth and Planetary Science Letters*, 403: 236–245,
1198 2014.
1199
1200 K.J. Walsh, A. Morbidelli, S.N. Raymond, D.P. O'Brien, and A.M. Mandell. A low
1201 mass for mars from Jupiter's early gas-driven migration. *Nature*, 475(7355):206–209,
1202 2011.
1203
1204 G. W. Wetherill. Occurrence of giant impacts during the growth of the terrestrial
1205 planets. *Science*, 228(4701):877-879, 1985.
1206
1207 J. Wade and B. J. Wood. Core formation and the oxidation state of the Earth. *Earth and*
1208 *Planetary Science Letters*, 236(1-2):78-95, 2005.

B. J. Wood, M. J. Walter, and J. Wade. Accretion of the Earth and segregation of its core. *Nature*, 441(7095):825–833, 2006.

B. J. Wood, J. Wade, and M. R. Kilburn. Core formation and the oxidation state of the Earth: Additional constraints from Nb, V and Cr partitioning. *Geochimica et Cosmochimica Acta*, 72(5):1415–1426, 2008.

Captions of Figures and Tables

Figure 1: Schematics of core-mantle segregation. First, the impactor (metal+silicate) enters a turbulent magma ocean. The impactor is fragmented and melted on impacting the surface of the proto-planet. The metallic phase then forms a diapir which, if the magma ocean is turbulent enough, fragments into a cloud of droplets ranging in size from a few millimeters to 10 cm maximum (Rubie et al., 2011; Deguen et al, 2014; Wacheul et al., 2014; Wacheul and Le Bars, 2017,2018). Each droplet interacts with the surrounding silicate, exchanging heat and chemical elements, until it reaches thermo-chemical equilibrium with its environment.

Figure 2: Schematic representation of the initial conditions and geometry of our models. The characteristics of the metal and silicate phases are listed respectively in red and black. The boundary conditions are detailed in blue (top), solid red line (side), green (bottom and global conditions). The red arrow illustrates the symmetry axis (red dotted line) used to define the 3D output.

Figure 3: Evolution of the metallic volume ratio ($V_{calculated}/V_{theoretical}$) during a simulation for different h_{max} values, for a silicate viscosity of 100 Pa.s. The colored and dashed line represent the evolution of $V_{calculated}/V_{theoretical}$ for different mesh sizes with time. The scale at the top shows the distance traveled by the diapir over a given time.

Figure 4: Evolution of the velocity field, r-component (on the left) and z-component (on the right), for different widths of computational domain. Widths vary from 2x R_{Fe} to 6x R_{Fe}. The chosen width for the simulations is 5xR_{Fe}. Note that the results presented here are calibration runs, with a height of 30x$R_{Fe.}$ The same simulations have been performed at varying heights, leading to a final height of 28x R_{Fe} (see Fig. 2 for the calibrated geometry).

Figure 5: Evolution of the volume fraction of the silicate during the simulation. When equal to 1 (red), the fluid is a silicate, when equal to 0 (blue) the fluid is a metal. The limit between metal and silicate is the black line between the red and blue parts (Φ_{ls} = 0.5). The time necessary for the diapir to reach the distance of 10R_{Fe} is 12.1 s.

Figure 6: Evolution of adimensional concentration of the siderophile element in the silicate, for a partition coefficient $D^{met/sil}$ = 1. For clarity purposes the metal is shown by the grey area surrounded by a black line. The black line is the boundary between metal and silicate and defines the surface where the exchange reaction happens. The adimensional concentration is given by the following formula given in Eq. (9). In this case X^0_{sil} =10^{-5}, X^0_{met} = 0.2 and $D^{met/sil}$ =1, and the chemical Peclet number is Pe~800**.**

Figure 7: Evolution of the volume of silicate undergoing reaction during the simulation. In red, the volume of silicate affected chemically. In blue, the volume of silicate unaffected by the passage of the diapir. The metal is colored in grey. The ratio R_C defined in the study corresponds to the volume of the red areas divided by the total volume of silicate (red + blue areas).

Figure 8: Evolution of R_C as a function of time in the reference case defined in the text ($\mu_{sil} = \mu_{met} = 100$ Pa.s). The four lines illustrate four different values of $D^{met/sil}$ ranging from 1 (black) to 10^3 (blue).

Figure 9: Evolution of the time necessary for the diapir to move through $10R_{Fe}$ as a function of the silicate viscosity. Black points are the values corresponding to each study. The red area corresponds to Stokes flows, and the blue area to intermediate flows. The clusters of black points correspond to the variation in velocity due to the variation in metal viscosity. The theoretical values are plotted in red and derived from equations (9) and (10). Typical times of diapir equilibrium, from Wacheul et al. (2014), are shown in blue. The size of the marker is scaled logarithmically on the chemical Peclet number, ranging from 8 (smallest) to 3000 (largest).

Figure 10: On the left: *Re* as a function of *We* obtained from our numerical simulations (one red circle for each calculation). The blue area shows the Intermediate regime flow, and the red area the Stokes regime flow. The dashed area illustrates the domain where diapirs are stable. On the right: Comparison between the geologically plausible values of *We* and *Re* for the Earth's magma ocean and the values covered by our study.

Figure 11: Evolution of R_C as a function of *Re* during the sinking of a 1cm-radius droplet for an adimensional time of 1. The Stokes flow regime (red area) and intermediate flow regime (blue area) are separated by a black vertical line at *Re*=1. The dot color characterizes different values for $D^{met/sil}$ ranging from 1 to 10^3. The size of the marker is scaled logarithmically on the chemical Peclet number, ranging from 8 (smallest) to 3000 (largest).

Figure 12: Evolution of R_C as a function of R_μ for 5 different metallic viscosities (shown in the 5 boxes), different values of $D^{met/sil}$ and obtained at a distance of $10R_{Fe}$. From top left to bottom panel the metallic viscosity increases from 0.1 Pa.s to 1000 Pa.s. The silicate viscosities corresponding to R_μ are indicated on the top x-axis. The size of the marker is scaled logarithmically with the chemical Peclet number, ranging from 8 (smallest) to 3000 (largest).

Figure 13: Evolution of log R_C as a function of the normalized surface (left panel) and evolution of the normalized surface as a function of R_μ (right panel) for models with $\mu_{silicate}$ = 0.1 Pa.s for the reference time defined in Fig. 9. The normalized surface of the diapir is the surface of the diapir in the simulation divided by $S_{theoretical} = 4\pi R_{Fe}^2$ (initial surface of the sphere).

Figure 14: log*Rc* calculated from the parameterization of Eq (11) vs log*Rc* obtained from the simulations. The red line is the 1:1 line (perfect fit), and the dashed lines bound the 5σ confidence interval.

Figure 15: Mantle fraction chemically contaminated by a moderately siderophile element after metallic core fragmentation as a function of the impactor size. In these figures we compute Eqs. 6, 11 and 12 using R_{Fe}=1cm, v_{diapir}=v_{stokes} and μ_{met}=0.1 Pa.s. The left panel shows the influence of the partition coefficient for a fixed viscosity ratio R_μ=1. The right panel shows the influence of the viscosity ratio for a fixed partition coefficient $D^{met/sil}$=100.

Figure 16: Evolution of Ni/Co ratio in the mantle after an impact as a function of the impactor size for different silicate viscosities (0.1 to 100 Pa.s). We represent here the variation of the Ni/Co ratio after the impact relative to the initial BSE concentration: $\Delta\left(\frac{Ni}{Co}\right) = 100 \times \frac{\left(\frac{Ni}{Co}\right)_{Final} - \left(\frac{Ni}{Co}\right)_{BSE}}{\left(\frac{Ni}{Co}\right)_{BSE}}$. Since the impact happens on the BSE, the more the Ni/Co ratio is different to that of the BSE, the more the impactor has reached equilibrium.

Figure 17: Ni/Co ratio in the Earth's mantle before equilibration with the core of an impactor corresponding to 10% of the Earth's mass as a function of the radius of the impactor's core normalized to the impactor size and for different magma ocean viscosities. The R_{core}/R_{Earth} current ratio is shown by the blue dashed line, and the R_{core}/R_{Mars} ratio by a red dashed line. In the calculation, the impactor is the same size as Mars ($R_{impactor}$ = 3390 km), and the impactor core radius ranges from 340 km to 2040 km. We represent here the variation in Ni/Co ratio before the impact relative to the BSE concentration but for a well-mixed mantle after impact: $\Delta\left(\frac{Ni}{Co}\right) = 100 \times \frac{(\frac{Ni}{Co})_{post-impact} - (\frac{Ni}{Co})_{BSE}}{(\frac{Ni}{Co})_{BSE}}$.

Table 1: Parameters and variables used in this study. When values are not given, the variable is calculated later in the text (according to the specific case).

Table 2. Values of fitted parameters for Eq. 11 using the least-square methods. The errors associated with the value are given by the 1σ error value. The data used for parameterization are the same as the data presented in sections 3.3 and 3.4. The comparison between calculated values from Eq. 11 and the values obtained after simulation is presented in Fig. 13.

1333 **Table 1**

Parameter	Name	Values in this study
All models		
ρ	Density of the fluid	silicate: 3300 - metal: 8000 kg.m^{-3}
t	Time	0.6 - 125 s
u	Velocity vector	m.s^{-1}
R_{Fe}	Radius of the diapir	1 cm
h_{max}	Maximum unit cell size	**0.1** × R_{Fe}
Two-phase flow		
P	Dynamic Pressure of the fluid	1 atm
μ	Dynamic viscosity of the fluid	10^{-1} – 10^{3} Pa.s
g	Acceleration of gravity	9.81 m.s^{-2}
l	Distance fluid - initial interface	m
F_{st}	Surface tension force	Calculated for σ = 1 N.m^{-1}, in N.m^{-3}
Φ	Volume fraction of the fluid	silicate: Φ =0 metal: Φ = 1 no unit
ϵ_{ls}	Parameter controlling interface reinitialization	$h_{max}/2$

γ	Parameter controlling velocity reinitialization	0.001 – 0.3 $m.s^{-1}$
Transport of Diluted Species		
c_i	Concentration of element i	$mol.m^{-3}$
k_c	Diffusion coefficient of element i	10^{-6} $m^2.s^{-1}$
R_i	Reaction rate for element i	$mol.m^{-3}.s^{-1}$
N_i	Molar flux of element i	0 $mol.m^{-2}.s^{-1}$
Scaling of the study		
Re	Reynolds number	2.5×10^{-5} to 110
We	Weber number	2.3×10^{-5} to 3.5
R_μ	Viscosity ratio ($= \mu_{met}/\mu_{sil}$)	10^{-4} to 10^{4}
R_C	Ratio of the silicate volume reacted	see Section 3

Table 2

Parameters	a (*Dmet/sil*)	b (*Re*)	c (R_μ)	d
Values	-0.235	-0.283	0.011	-1.686
1σ	0.02	0.03	0.001	0.07

1336

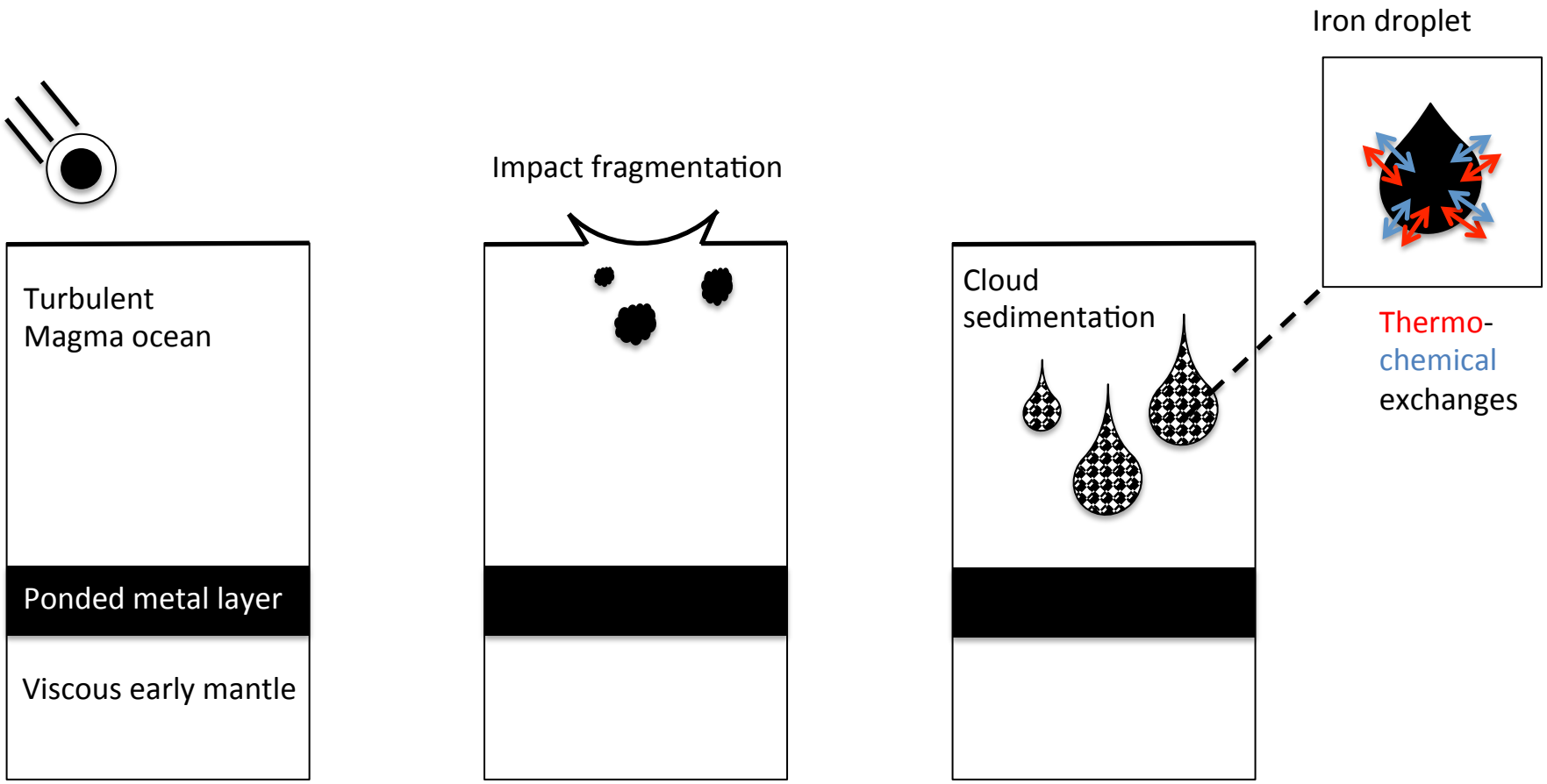
Turbulent
Magma ocean
Ponded metal layer
Viscous early mantle
Impact fragmentation
Cloud
sedimentation
Iron droplet
Thermo-
chemical
exchanges

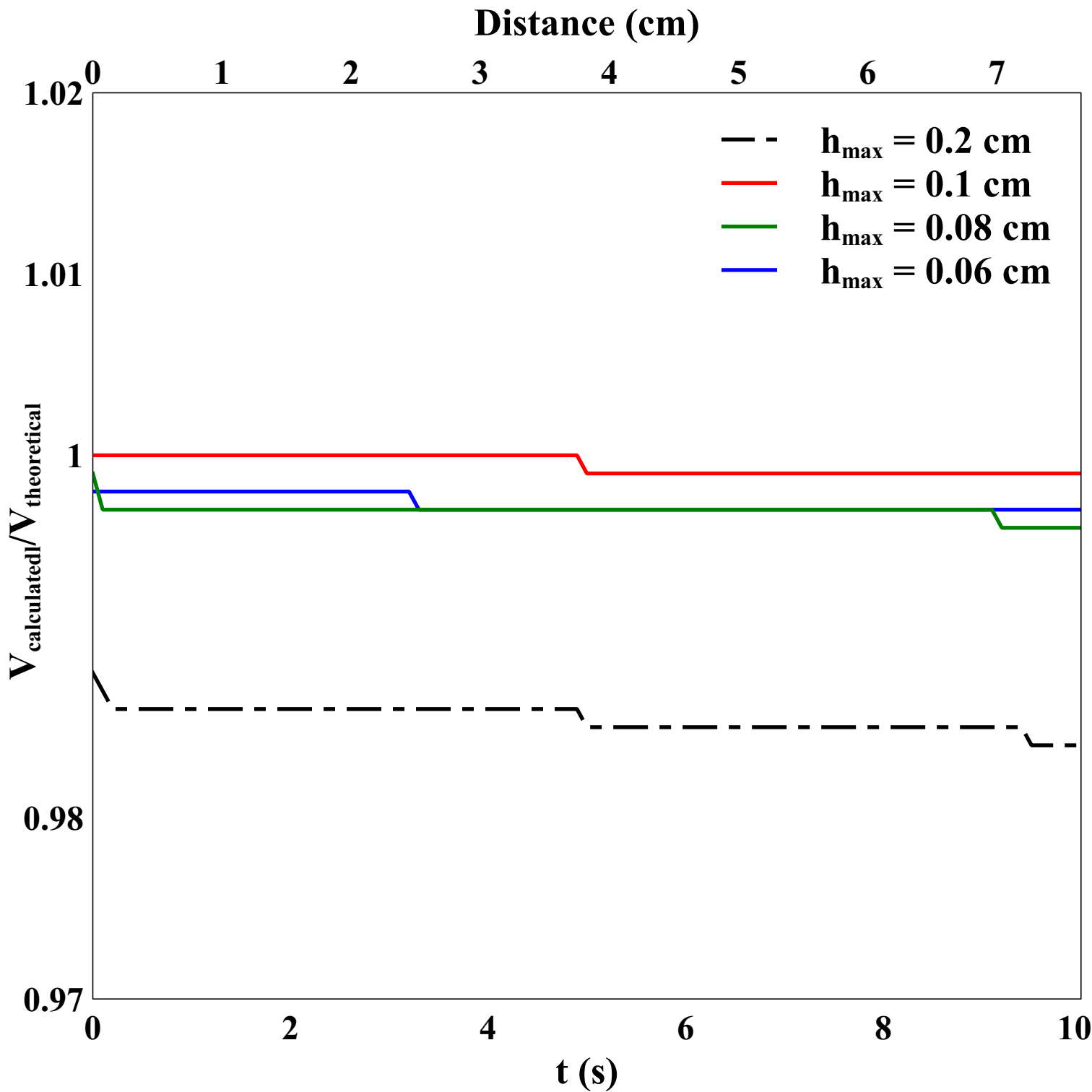
Distance (cm)
0
1
2
3
4
5
6
7
1.02
1.01
1
0.98
0.97
$V_{calculated}/V_{theoretical}$
h_{max} = 0.2 cm
h_{max} = 0.1 cm
h_{max} = 0.08 cm
h_{max} = 0.06 cm
0
2
4
6
8
10
t (s)

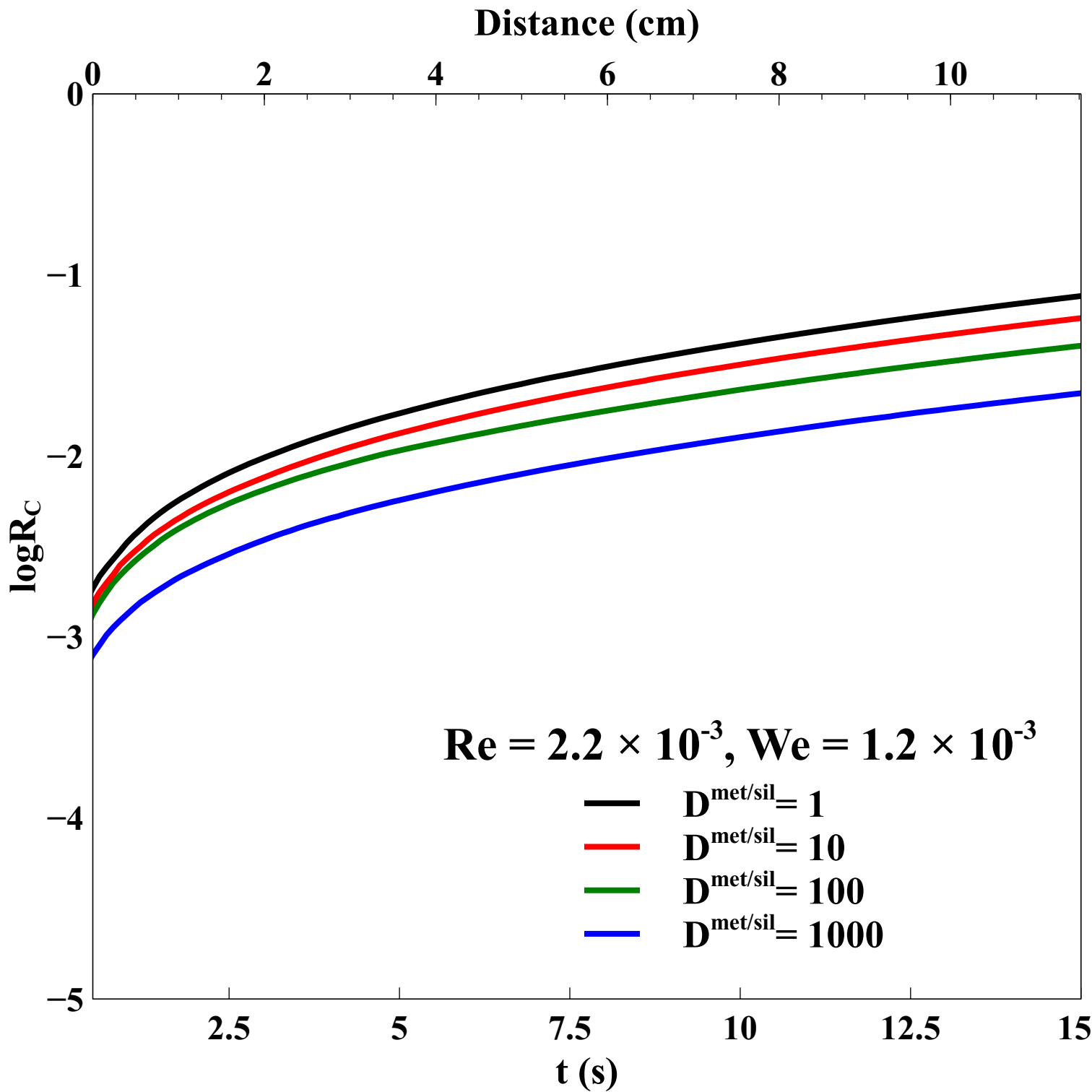
Distance (cm)
0
2
4
6
8
10
0
−1
−2
−3
−4
−5
logR_C
Re = 2.2 × 10^-3, We = 1.2 × 10^-3
D^met/sil = 1
D^met/sil = 10
D^met/sil = 100
D^met/sil = 1000
2.5
5
7.5
10
12.5
15
t (s)

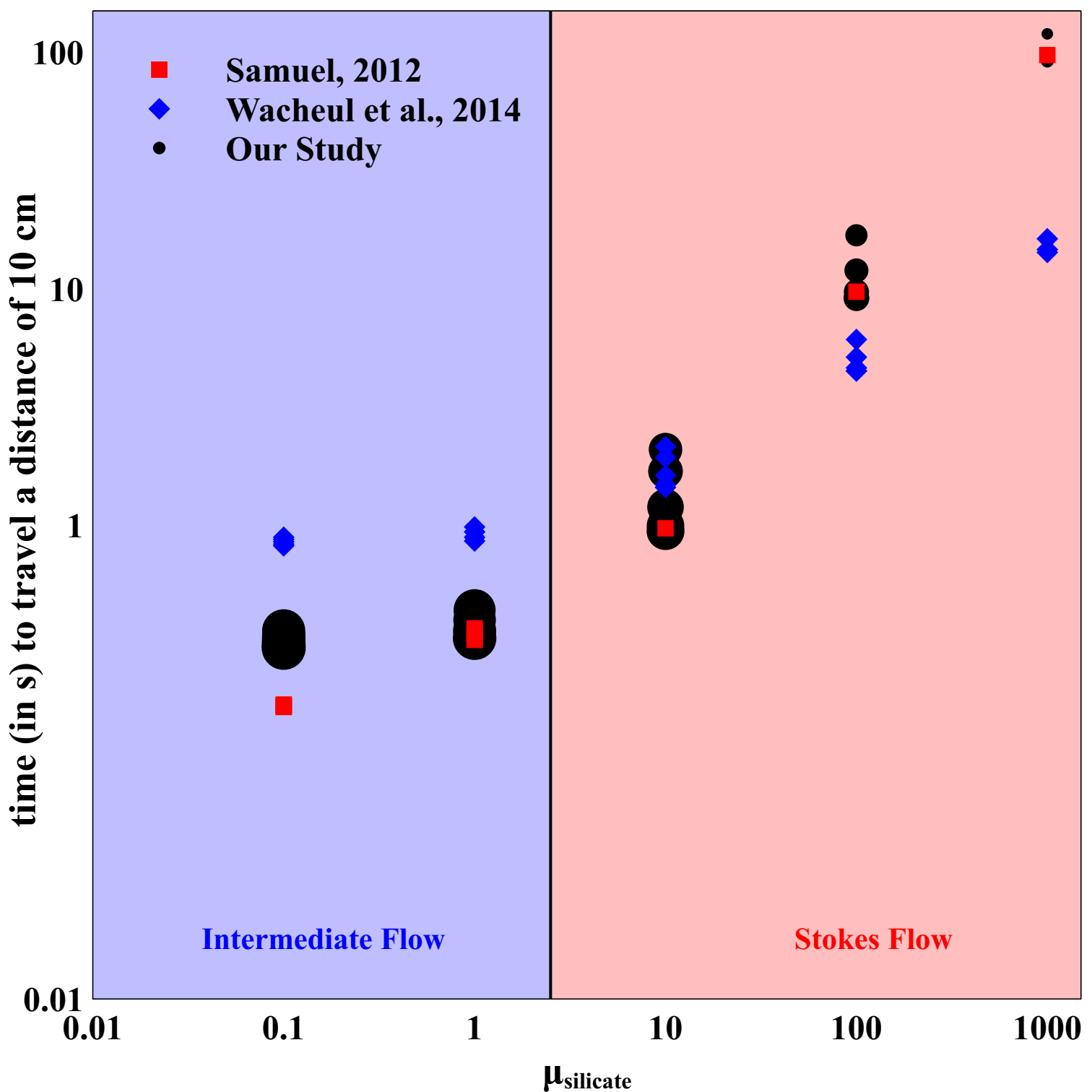
Samuel, 2012
Wacheul et al., 2014
Our Study
Intermediate Flow
Stokes Flow
time (in s) to travel a distance of 10 cm
100
10
1
0.01
0.01
0.1
1
10
100
1000
μsilicate

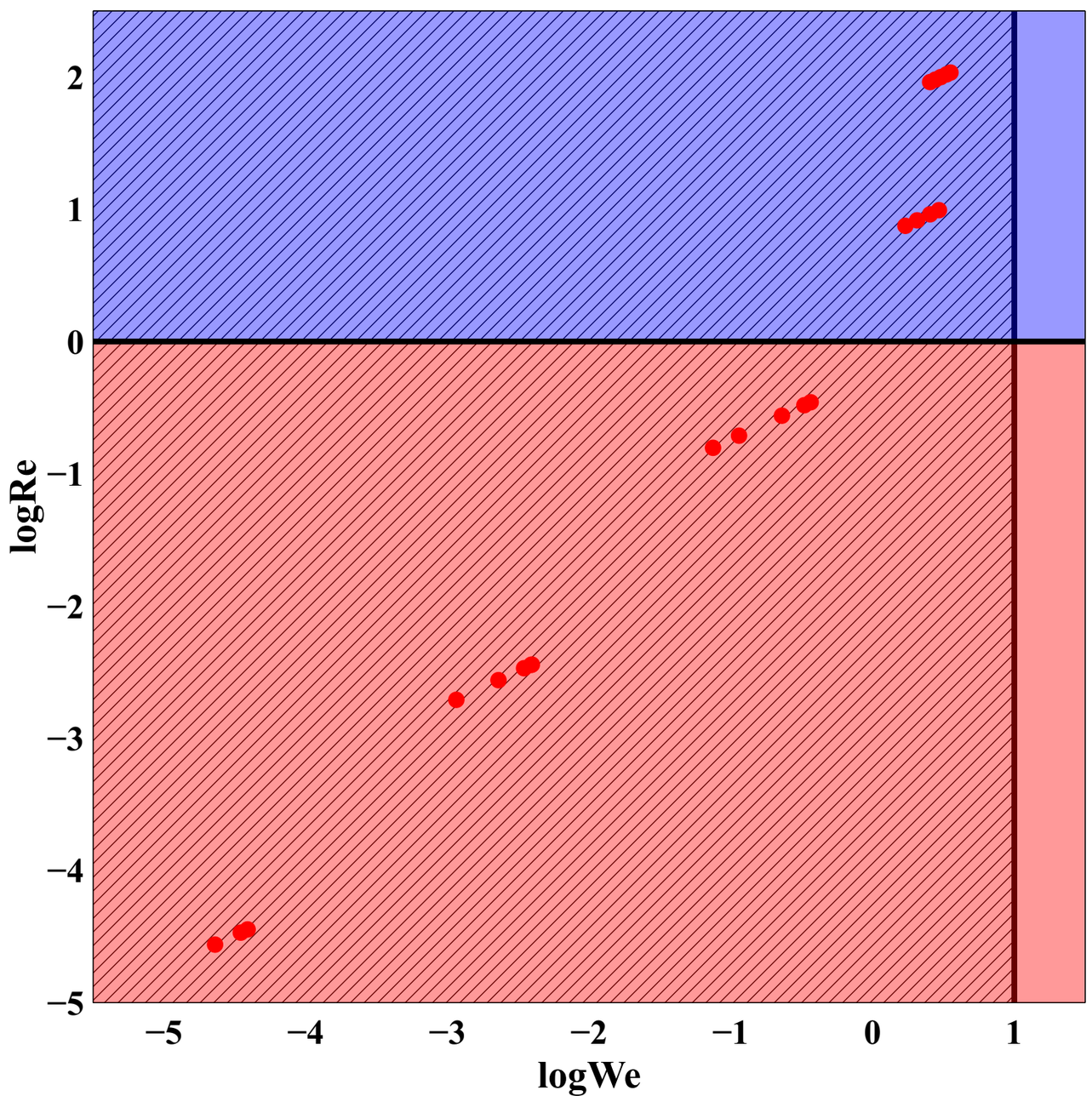
2
1
0
−1
−2
−3
−4
−5
logRe
−5
−4
−3
−2
−1
0
1
logWe

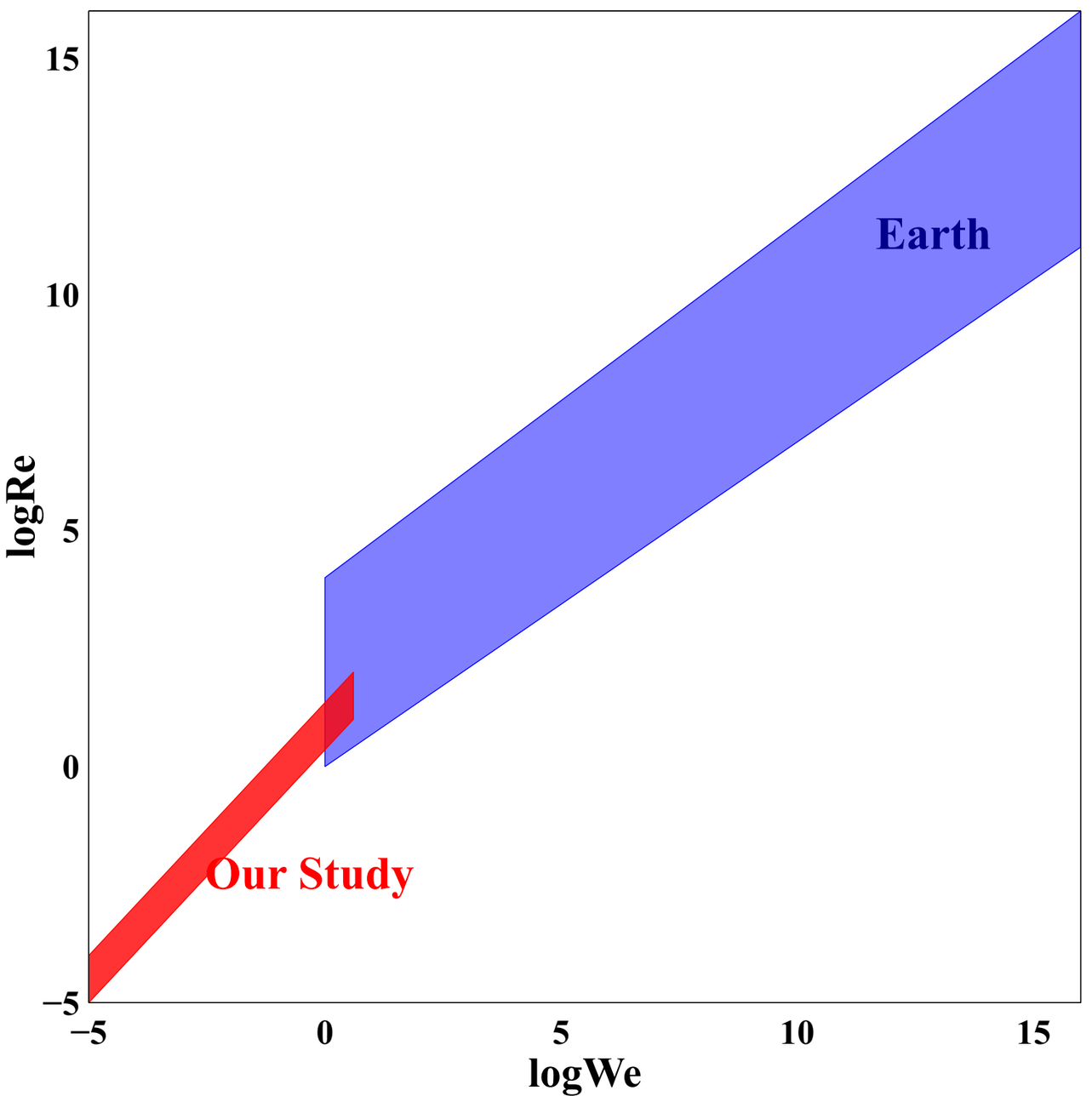
15
10
5
0
−5
logRe
Earth
Our Study
−5
0
5
10
15
logWe

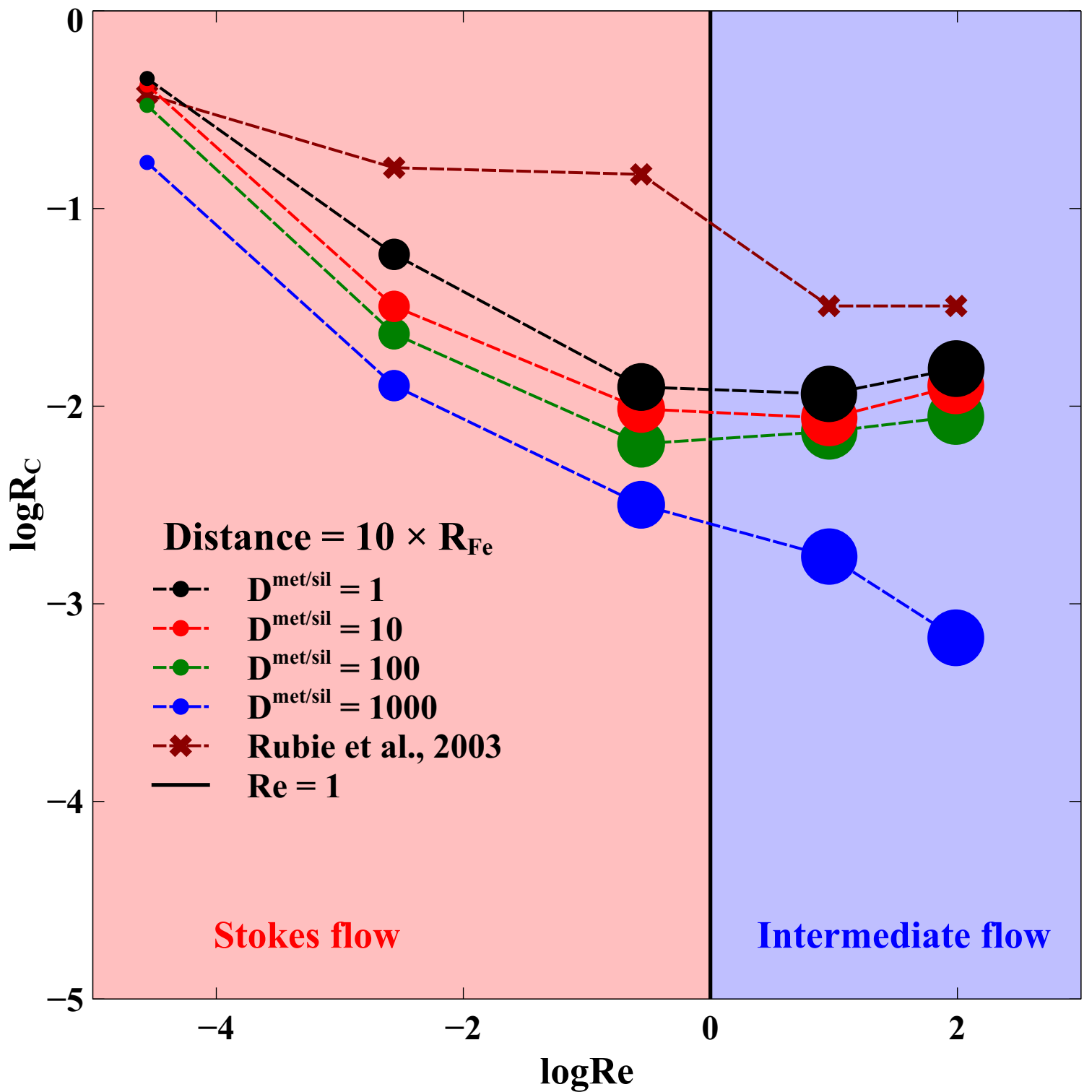
0
−1
−2
−3
−4
−5
logR_C
−4
−2
0
2
logRe
Distance = 10 × R_Fe
D^met/sil = 1
D^met/sil = 10
D^met/sil = 100
D^met/sil = 1000
Rubie et al., 2003
Re = 1
Stokes flow
Intermediate flow

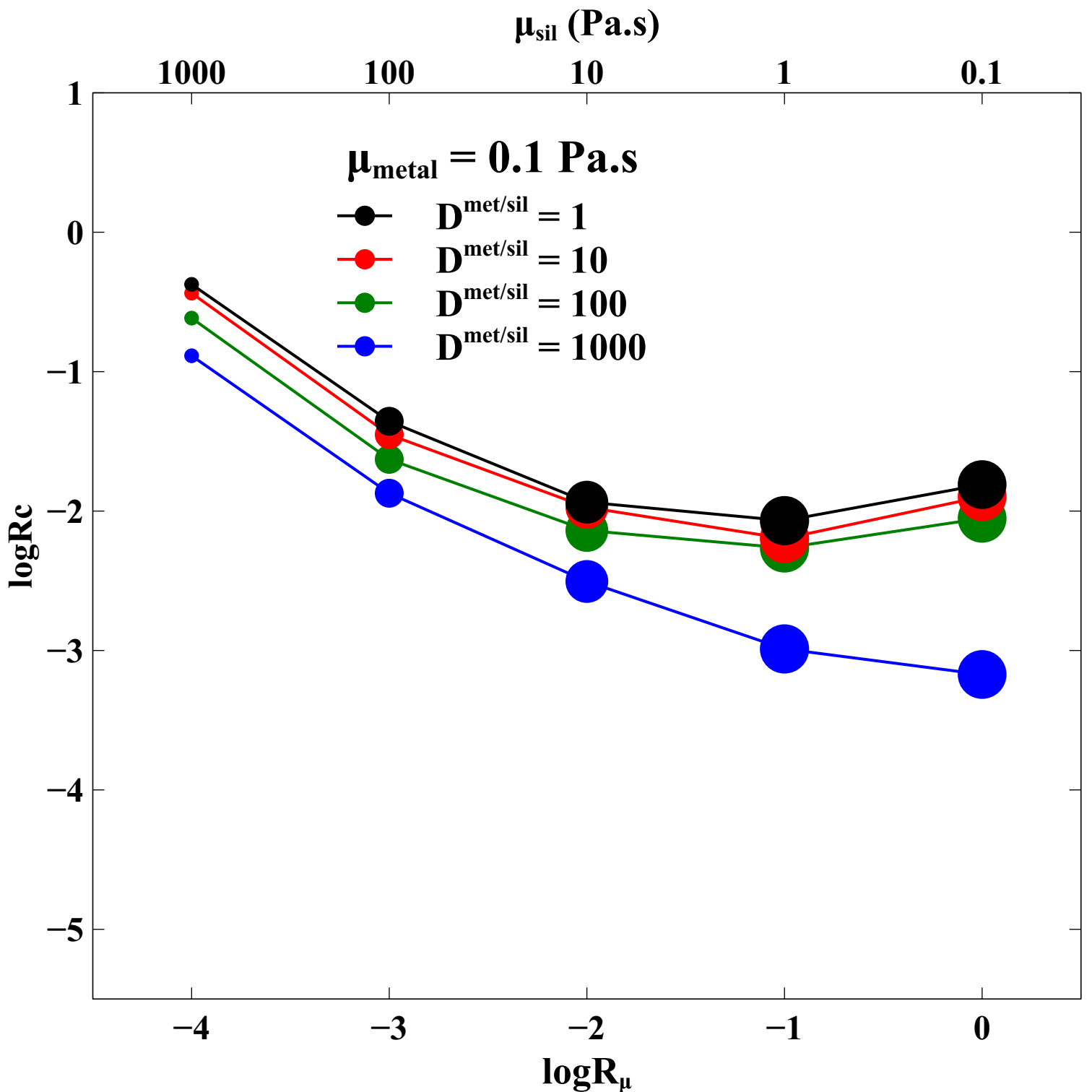
μsil (Pa.s)
1000
100
10
1
0.1
μmetal = 0.1 Pa.s
D met/sil = 1
D met/sil = 10
D met/sil = 100
D met/sil = 1000
logRc
logRμ
1
0
−1
−2
−3
−4
−5
−4
−3
−2
−1
0

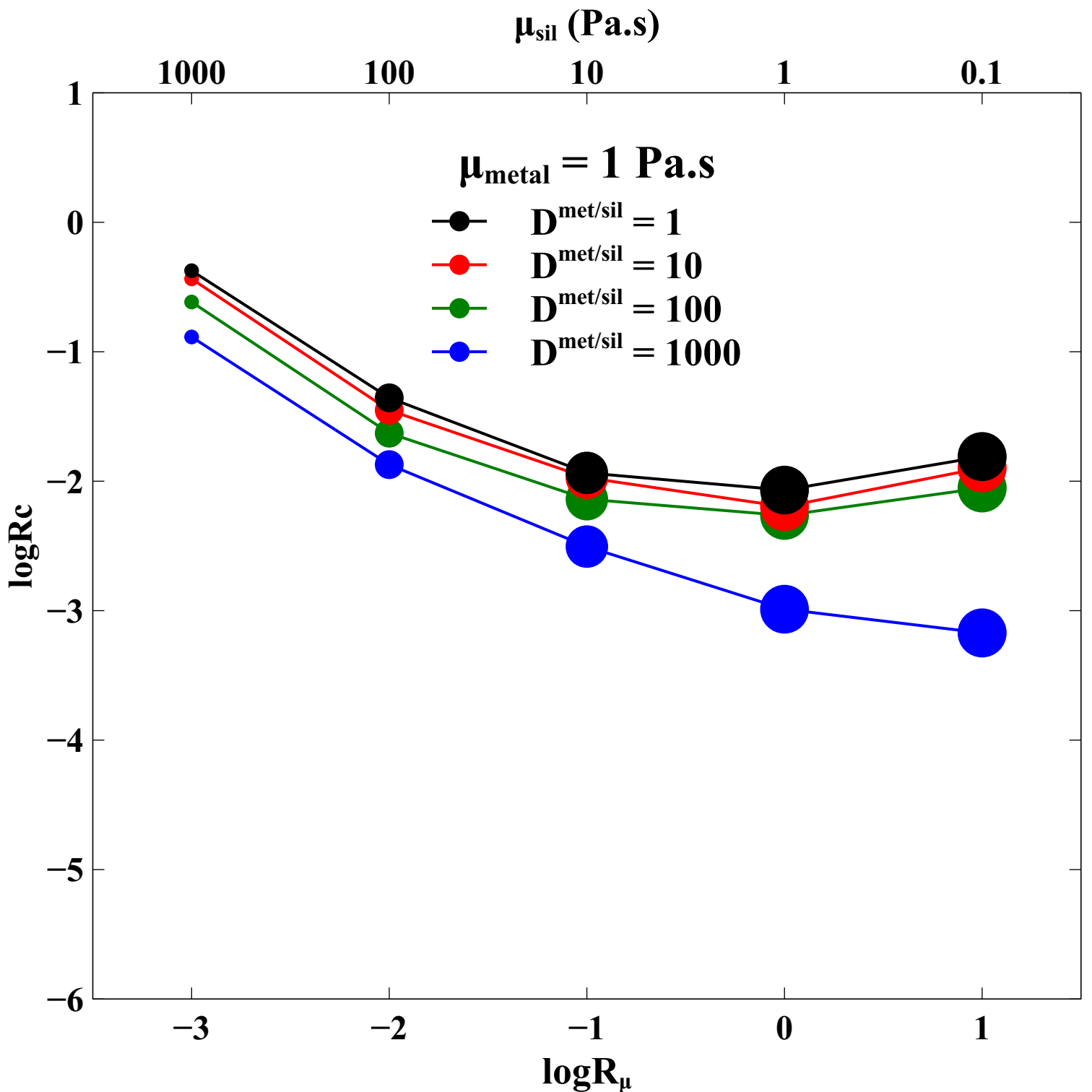
μsil (Pa.s)
1000
100
10
1
0.1
μmetal = 1 Pa.s
D met/sil = 1
D met/sil = 10
D met/sil = 100
D met/sil = 1000
logRc
logRμ
1
0
−1
−2
−3
−4
−5
−6
−3
−2
−1
0
1

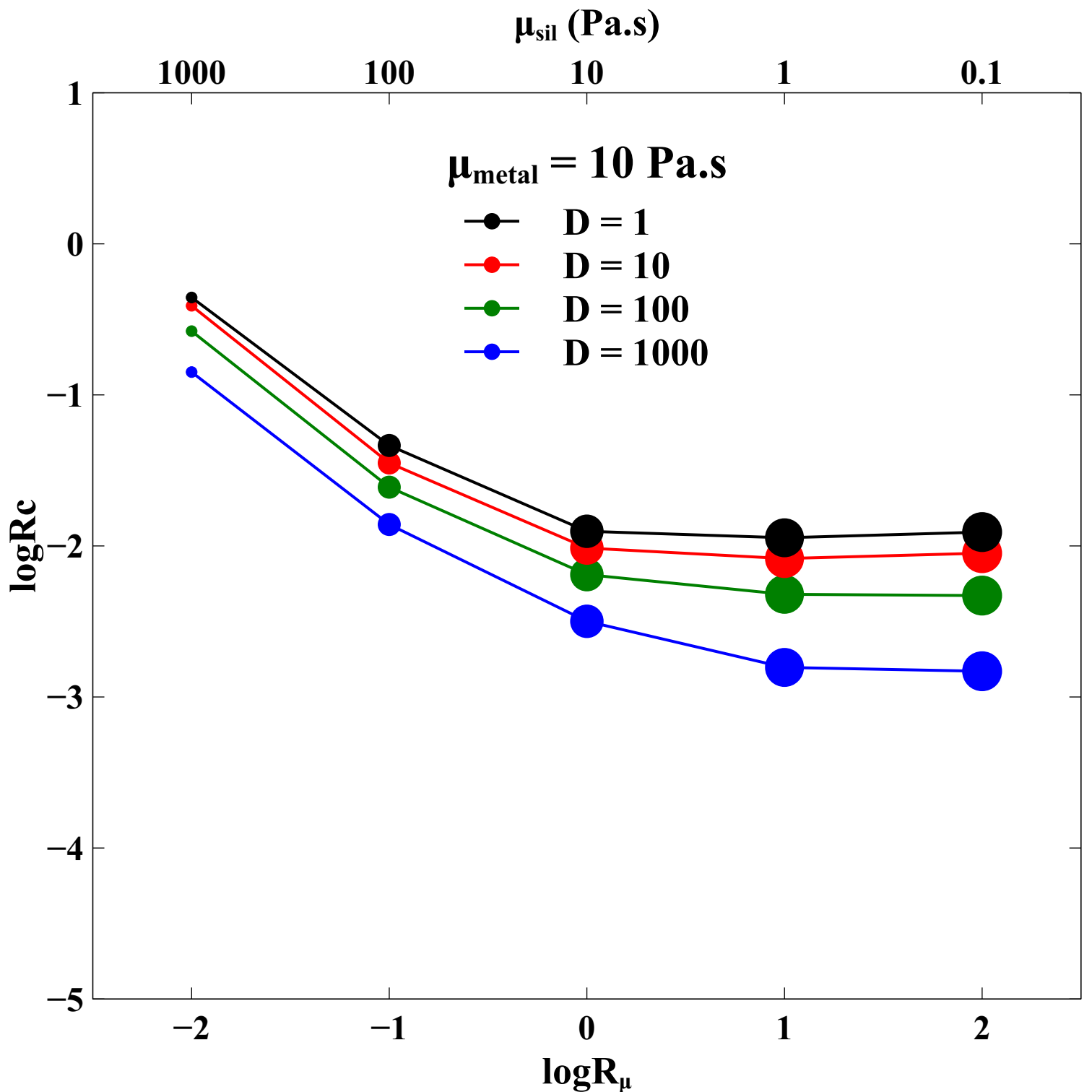
μsil (Pa.s)
1000
100
10
1
0.1
μmetal = 10 Pa.s
D = 1
D = 10
D = 100
D = 1000
logRc
logRμ
1
0
−1
−2
−3
−4
−5
−2
−1
0
1
2

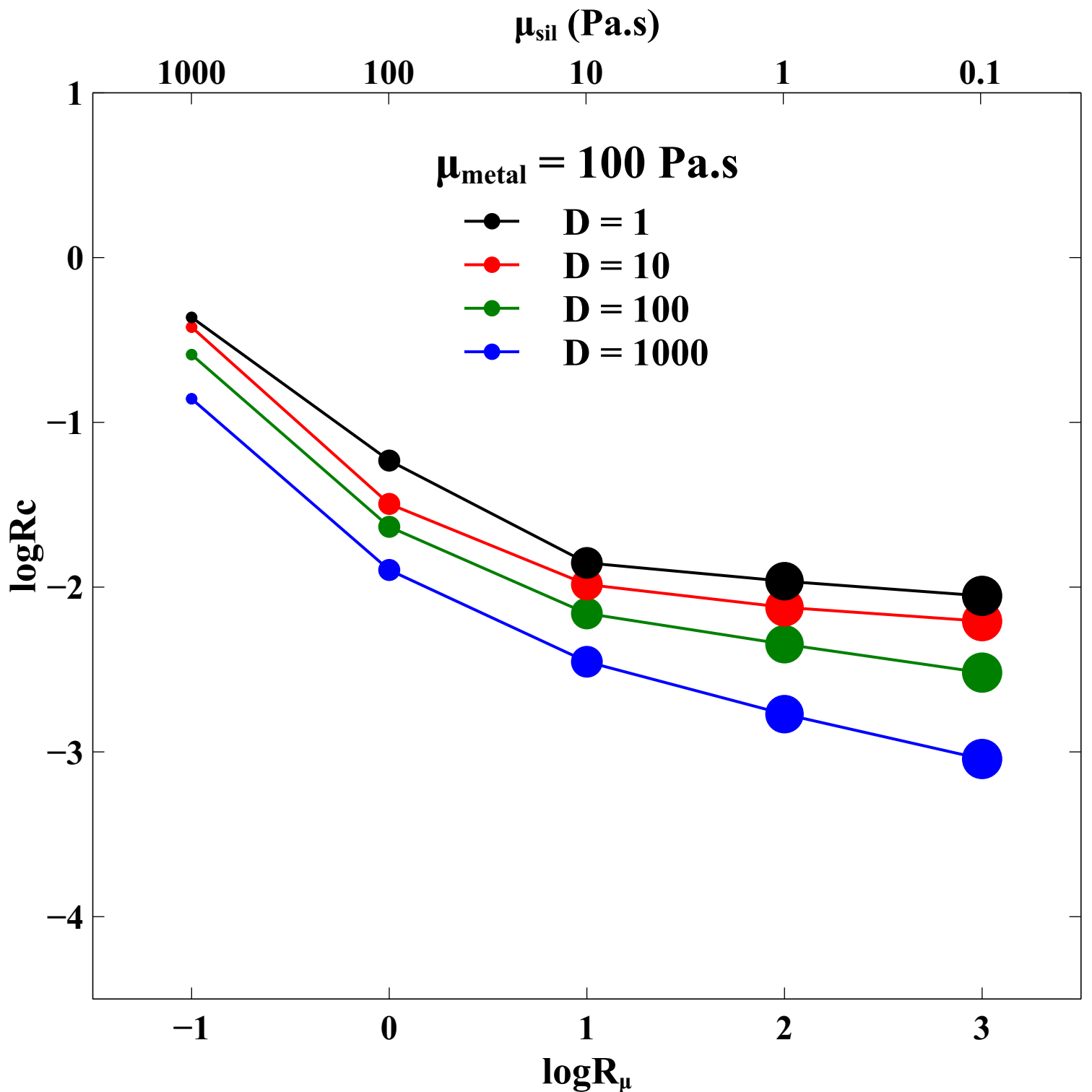
μsil (Pa.s)
1000
100
10
1
0.1
μmetal = 100 Pa.s
D = 1
D = 10
D = 100
D = 1000
logRc
logRμ
1
0
−1
−2
−3
−4
−1
0
1
2
3

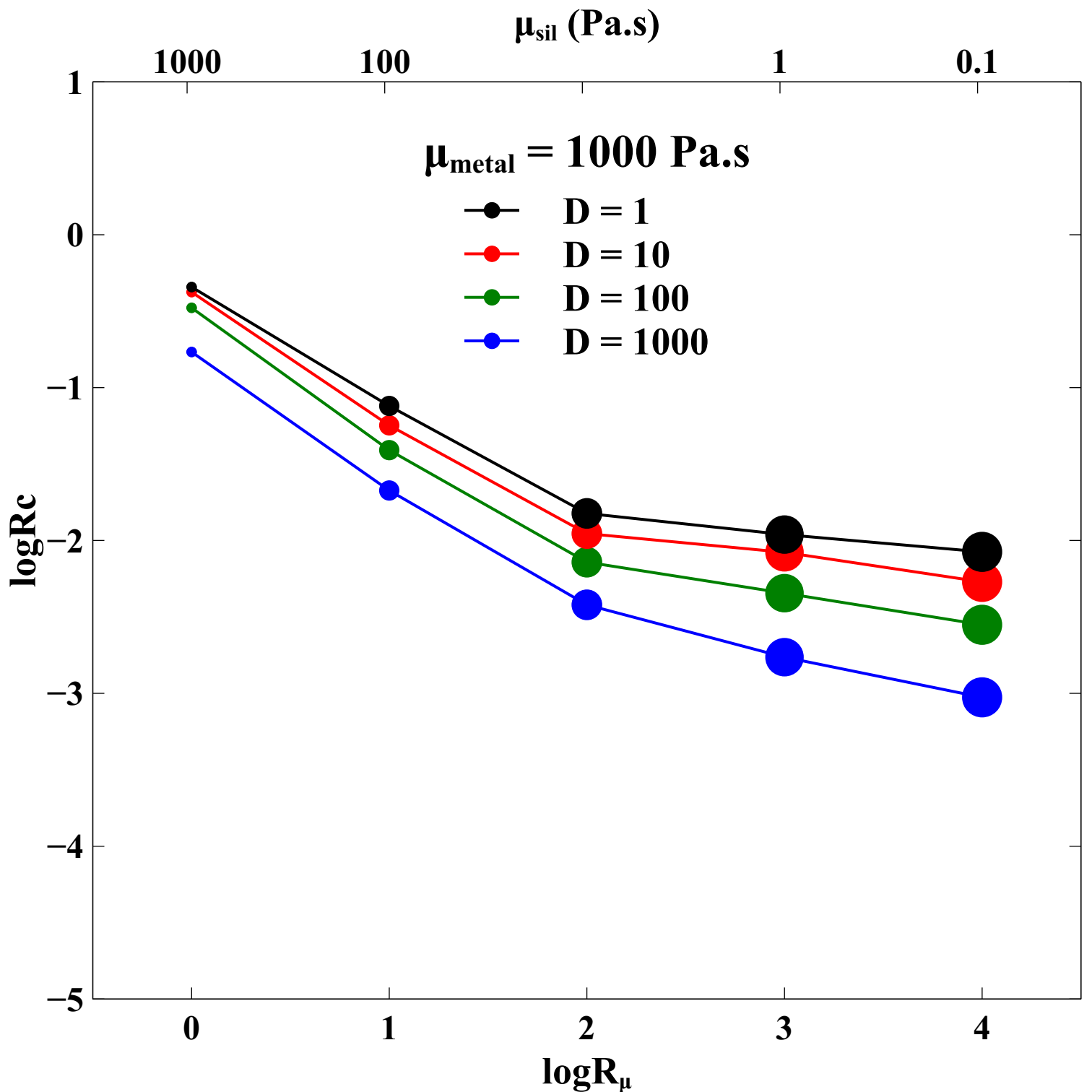
μsil (Pa.s)
1000
100
1
0.1
μmetal = 1000 Pa.s
D = 1
D = 10
D = 100
D = 1000
logRc
logRμ
1
0
−1
−2
−3
−4
−5
0
1
2
3
4

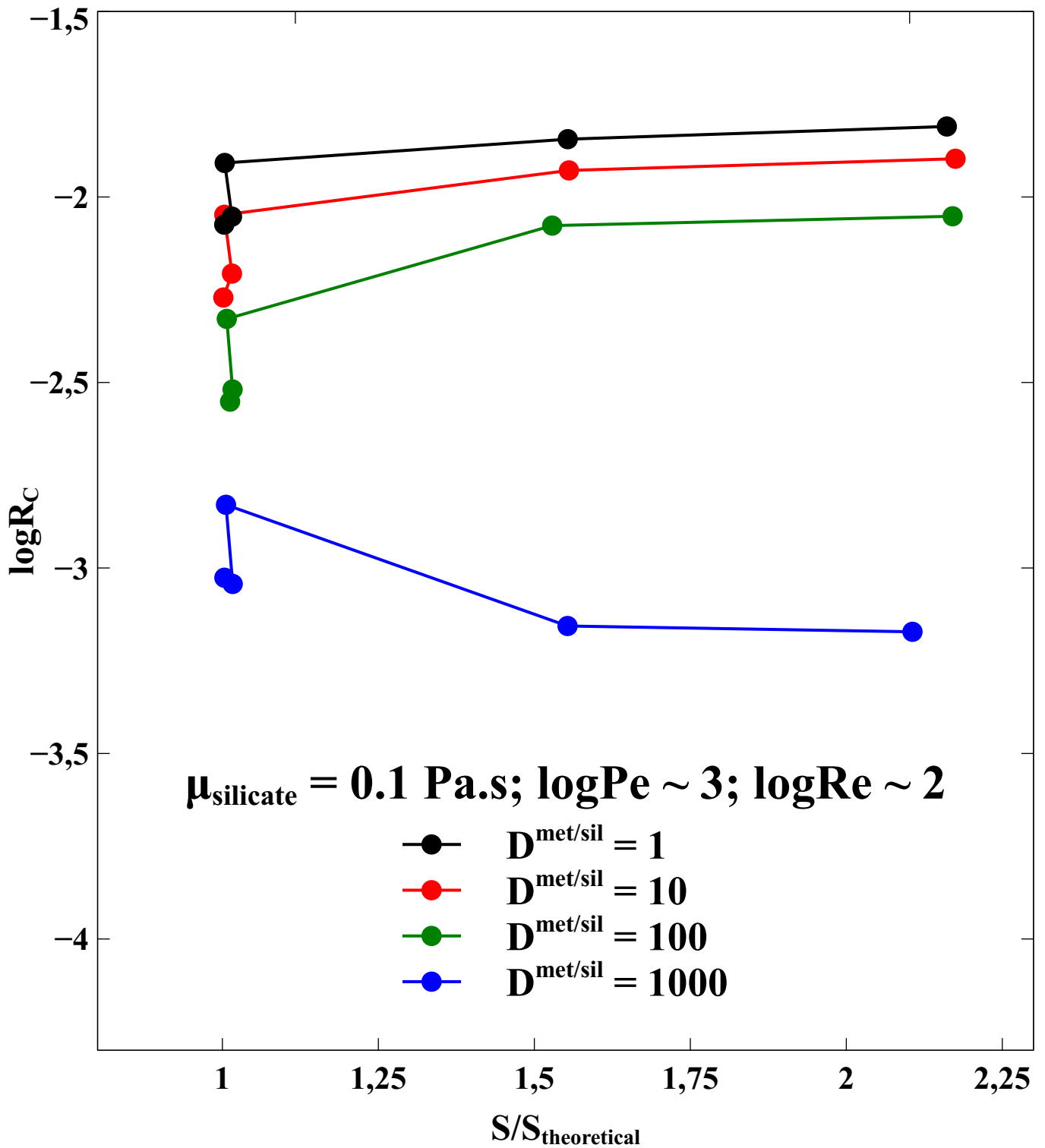
−1,5
−2
−2,5
−3
−3,5
−4
logR_C
μ_silicate = 0.1 Pa.s; logPe ~ 3; logRe ~ 2
D^met/sil = 1
D^met/sil = 10
D^met/sil = 100
D^met/sil = 1000
1
1,25
1,5
1,75
2
2,25
S/S_theoretical

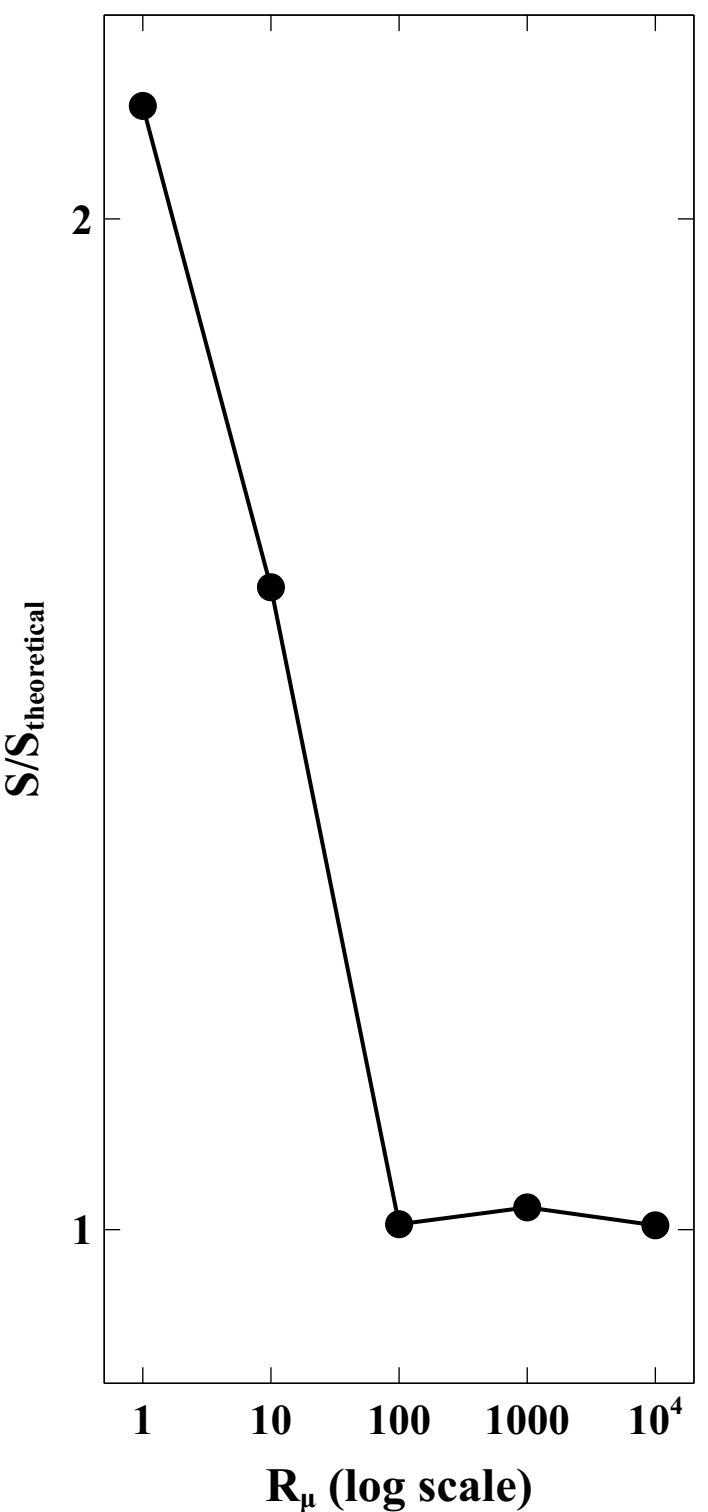
2
1
S/S_theoretical
1
10
100
1000
10^4
R_μ (log scale)

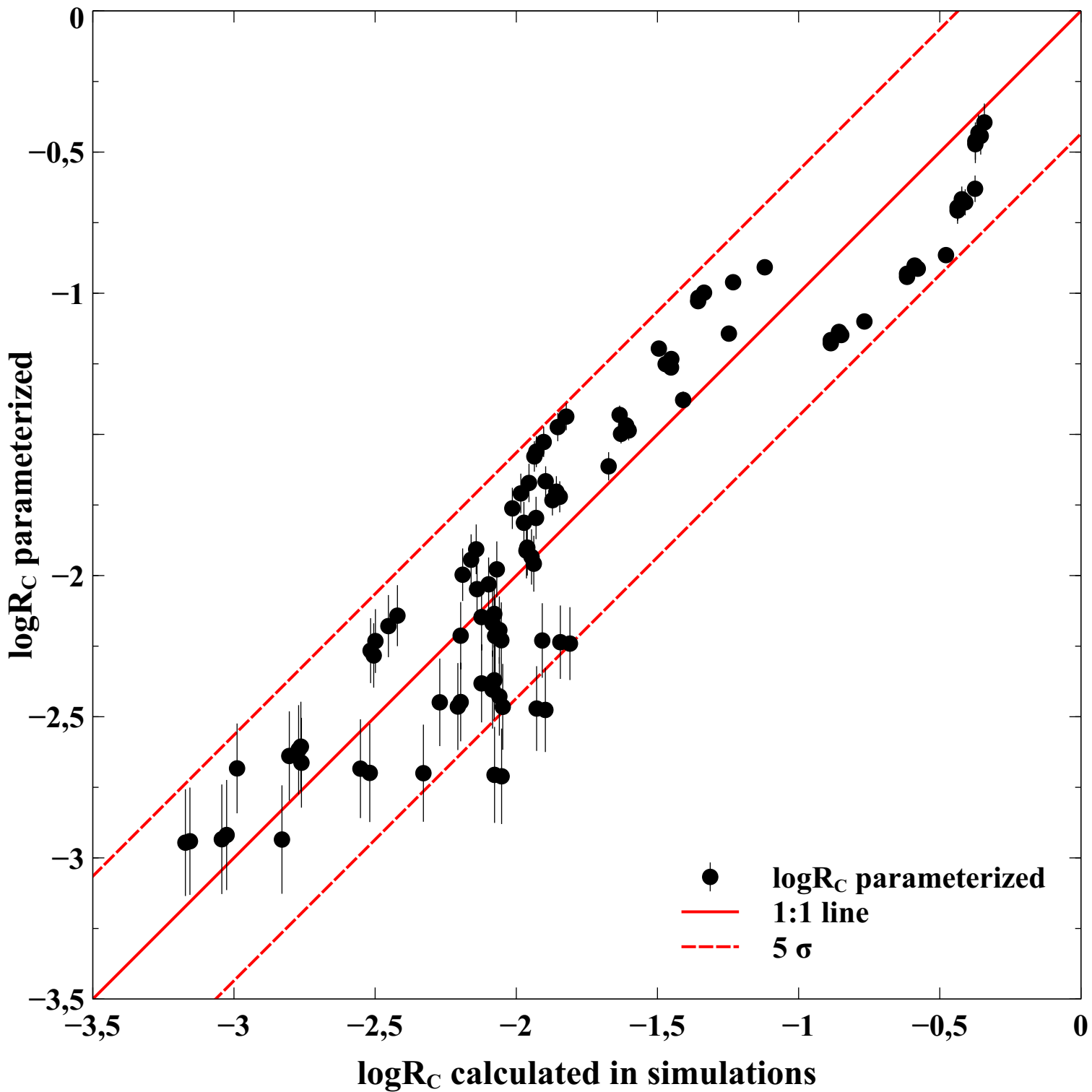
0
−0,5
−1
−2
−2,5
−3
−3,5
−3,5
−3
−2,5
−2
−1,5
−1
−0,5
0
logR_C parameterized
logR_C calculated in simulations
logR_C parameterized
1:1 line
5 σ

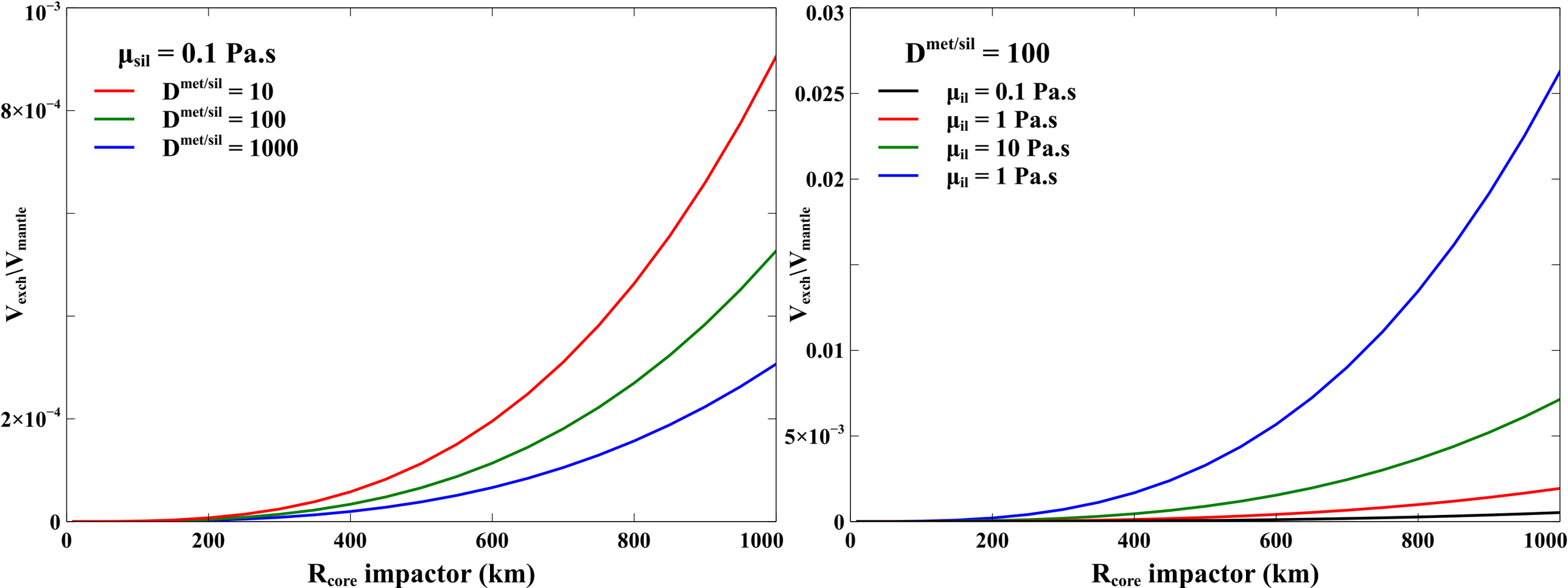
μ_{sil} = 0.1 Pa.s
$D^{met/sil}$ = 10
$D^{met/sil}$ = 100
$D^{met/sil}$ = 1000
V_{exch}/V_{mantle}
R_{core} impactor (km)
$D^{met/sil}$ = 100
μ_{il} = 0.1 Pa.s
μ_{il} = 1 Pa.s
μ_{il} = 10 Pa.s
μ_{il} = 1 Pa.s
V_{exch}/V_{mantle}
R_{core} impactor (km)

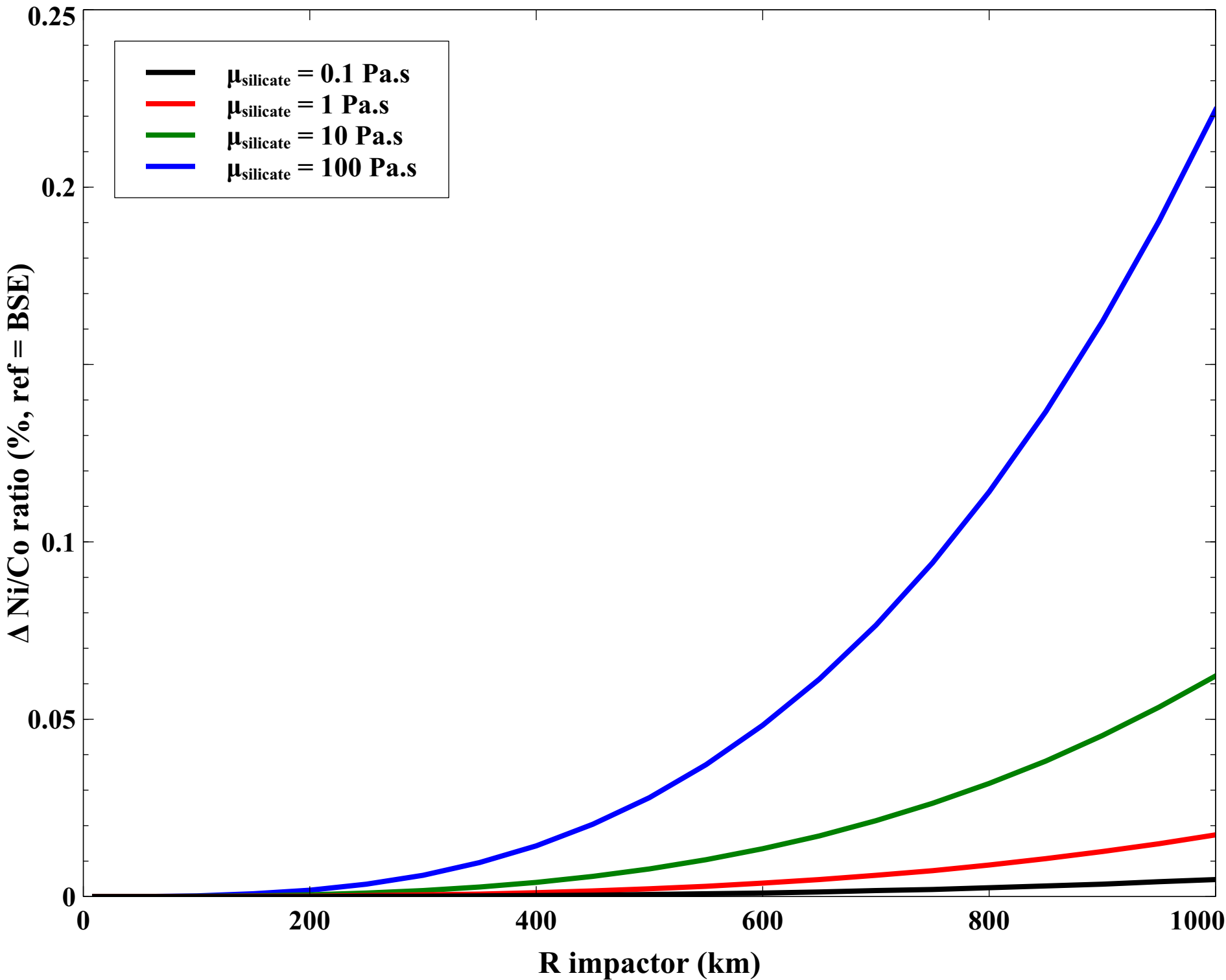
μsilicate = 0.1 Pa.s
μsilicate = 1 Pa.s
μsilicate = 10 Pa.s
μsilicate = 100 Pa.s
Δ Ni/Co ratio (%, ref = BSE)
0.25
0.2
0.1
0.05
0
0
200
400
600
800
1000
R impactor (km)

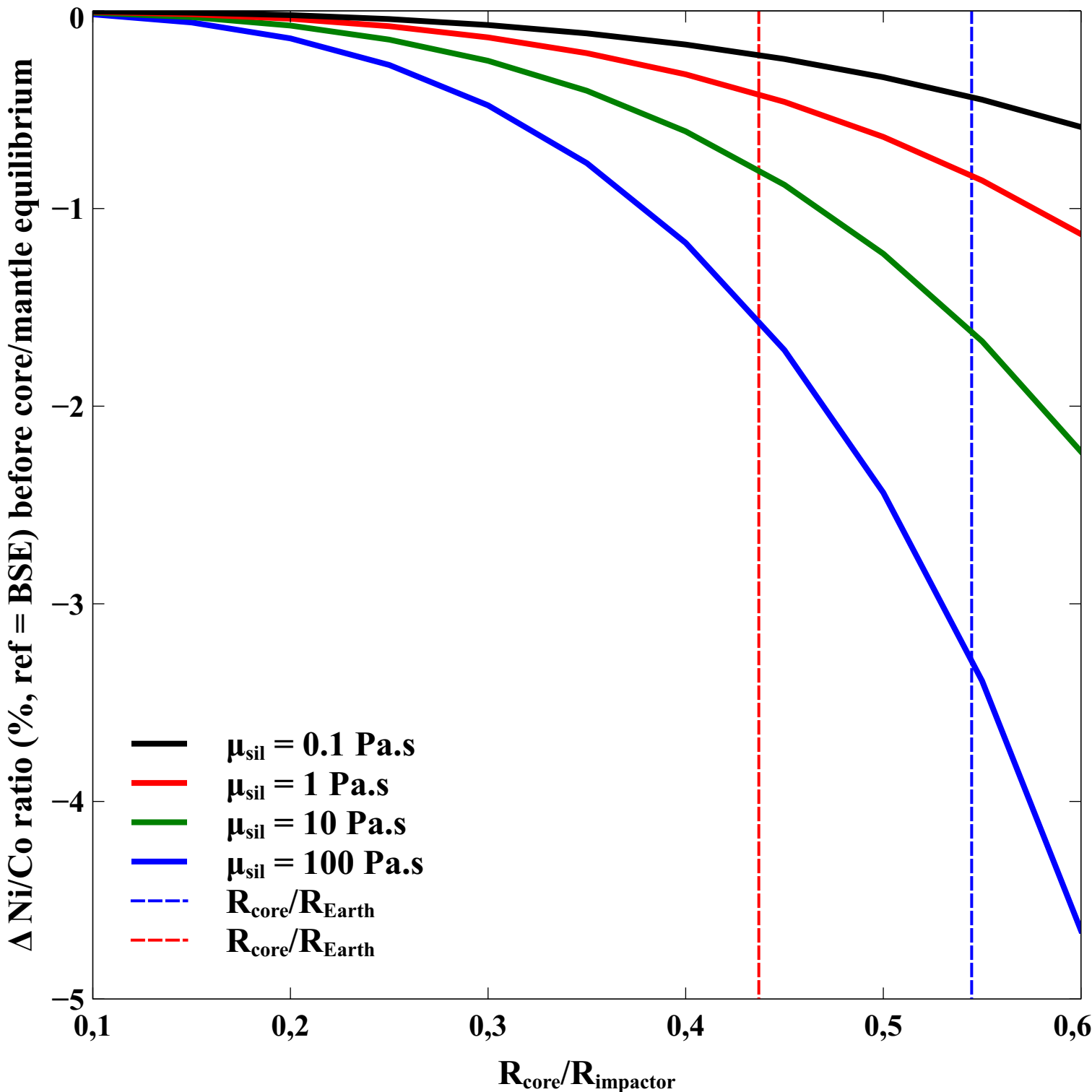
0
−1
−2
−3
−4
−5
0,1
0,2
0,3
0,4
0,5
0,6
Δ Ni/Co ratio (%, ref = BSE) before core/mantle equilibrium
R_core/R_impactor
μ_sil = 0.1 Pa.s
μ_sil = 1 Pa.s
μ_sil = 10 Pa.s
μ_sil = 100 Pa.s
R_core/R_Earth
R_core/R_Earth